공학박사학위논문

# Modelling and Analysis of Nanoparticles Transport in a Microfluidic channel for Enhancing the Sensitivity of Immunoassay

## 면역진단의 민감도 향상을 위한 미세유로에서의 나노 입자 유동 모델링 및 분석

**2020 년 8 월**

서울대학교 대학원
기계항공공학부
최 성 학

# Abstract

This study analyses the binding characteristics of analytes in a microfluidic channel using nanoparticles in order to provide design parameters and establish a database for biosensor. Sample containing model analytes flowed along the microfluidic channel and the binding characteristics are analyzed experimentally by counting the number of analytes bound to the receptors according to the analyte concentration, sample flow rate, and the dimension of the microfluidic channel. A mathematical model for the transport of analytes is also presented based on a probability density function for Brownian motion. The empirical coefficient for the mathematical model is obtained using the experimental results, which remains valid for all different parameters such as analyte concentration, sample flow rate, and the observation position so that the generality of the model is verified. The results show the number of binding efficiency increases as the flow rate decreases and the observation position is closer to the inlet, but it is consistent with the concentration of the sample. The binding characteristics according to the dimension of the microfluidic channel are investigated with the mathematical model and the critical height is dependent on the observation position.

A simple method for enhancing the sensitivity of immunoassay is also presented by agitating the flow using dummy particles. By adding dummy particles into the sample, the transport of analytes towards receptors is enhanced and the effect of dummy particles increases as the volume fraction or size of dummy particles increases and the flow

rate of sample increases. The improved value is analyzed through numerical simulation which shows valid estimation comparing with the experimental results.

**Keyword** : Biosensor, Sensitivity of immunoassay, Transport of analyte, Microfluidic channel for biosensor
**Student Number** : 2013-23837

# Table of Contents

# Chapter 1. Introduction

## 1.1. Biosensor

### 1.1.1. Biosensing

The biosensor has various applications such as early diagnosis of diseases or blood glucose monitoring for diabetes and its global market is growing very fast fueled by point-of-care [1-1].

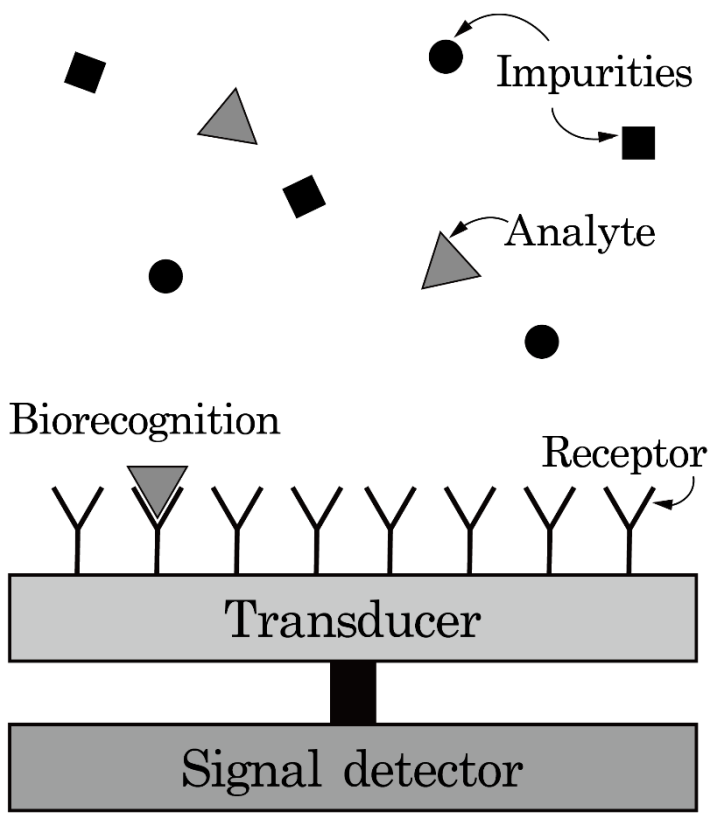


Figure 1-1. Structure of biosensor.

The biosensor is a three-elements system consisting of a bioreceptor, a transducer, and a signal processing unit for detecting a specific target analyte [1-2], as shown in Figure 1-1. The analyte is a target substance that needs to be detected such as protein, antigen, or bacteria and it is recognized by a target molecule, specifically, which is known as a receptor such as enzymes, aptamer, or antibody. This recognition generated by the specific binding between the analyte and receptor is termed bio-recognition [1-3]. The bio-recognition is converted to a measurable signal by a transducer and the signal processing unit reads and displays this signal.

### 1.1.2. Characteristics of a biosensor

Biosensors share common attributes, among which three-most-important properties are selectivity, sensitivity, and linearity [1-3]. In order to detect only a target analyte, biosensors must have selectivity and it is capable through the specific binding between analytes and bioreceptors such as antigen-antibody. The sensitivity of a biosensor is normally evaluated by the limit of detection which is the minimum amount of analytes that can be detected by the sensor [1-4]. Especially, in medical diagnostics fields, the limit of detection is required to be ng/ml or even pg/ml for early diagnosis or precise analysis because the sample solution like blood commonly contains low-concentration of analytes. The linearity indicates the accuracy of the measured signal represented as $y=mc$, where y is the output signal, m is the sensitivity of the sensor, and c is the concentration of analyte [1-3]. In order to estimate the amount and concentration of analyte from the signal transduced by the biorecognition, the

linearity of a sensor should be maintained under test.

### 1.1.3. Classification of biosensors

The biosensors are commonly classified by the signal transduction perspective or the bio-recognition perspective. Several examples are illustrated in Table 1-1 according to these two factors [1-5].

Table 1-1. Biosensor classification [1-5].

| *Recognizing biomolecule* | *Example* | *Signal transduction* | *Example* |
|---|---|---|---|
| Antibodies (Immunosensors) | *Monoclonal*<br>*Polyclonal* | Electrochemical | Amperometric<br>Conductimetric<br>Impedimetric<br>Potentiometric |
| Protein receptors | *Metabotropic receptors*<br>*Ionotropic receptors* | Optical | *Absorbance*<br>Fluorescence<br>Phosphorescence<br>Bio/chemiluminescence<br>Reflectance<br>Raman scattering<br>Refractive index |
| Enzymes | $\beta$-glucuronidase (encoded by *gusA* marker gene)<br>$\beta$-galactosidase (encoded by *lacZ* marker gene) | Mass sensitive | Surface acoustic wave biosensor<br>Cantilever biosensors |
| Whole cells | Microbial sensors<br>Mammalian cells tissue | Optical | *E. coli* K12C600<br>*E. coli* HB101<br>*E. coli* DPD1718 |
| Nucleic acids | Hybridization<br>DNA-aptamers based biosensors | Optical (Fluorescence) | Fluorescence-based aptasensor |

Based on the way of signal transduction, the biosensors are typically categorized into an electrochemical biosensor, thermal biosensor, optical biosensor, and mass-sensitive sensor. The most widespread biosensor is optical biosensor which is represented by surface plasmon resonance (SPR). As shown in Figure 1-2, optical biosensor accounts for nearly 80 % of the biosensor in the antibacterial field, containing the SPR technique [1-6]. The optical sensor has distinct advantages such as rapid detection time,

portability, cost-effective diagnostics, which are regarded as the most important characteristics in the recent biosensor market [1-7].

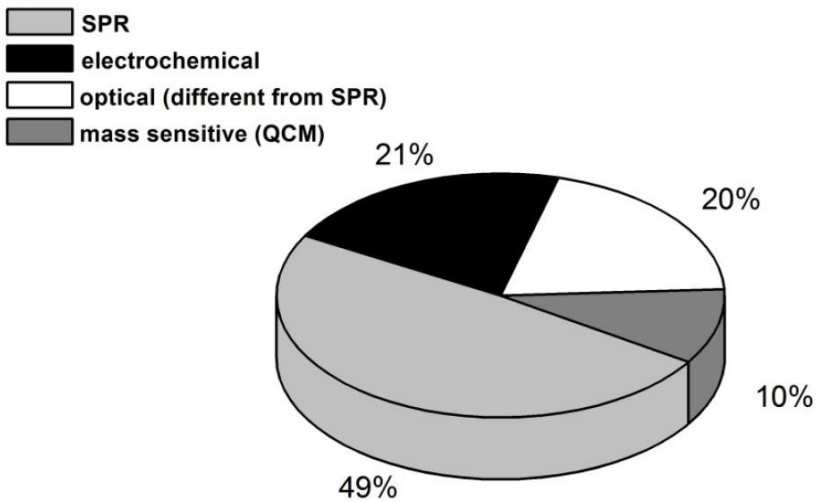


Figure 1-2. Biosensor applications classified regarding to the detection principles [1-6].

Biosensors are also classified into an enzymatic biosensor, protein-receptor based biosensor, immunoassay based biosensor, DNA biosensor, and whole-cell based biosensor based on the biorecognition principle [1-5]. In the case of the enzymatic biosensor, the native enzyme can be used as an analyte and the enzyme can be attached to the bioreceptor as a label for biorecognition [1-8]. Most of the signals for the enzymatic biosensor are provided electrochemically. Protein-based receptors such as metabotropic or ionotropic receptor located at the cell membrane generate biorecognition signals which are transduced through the membrane [1-9]. Receptors for immunoassay based biosensors are immobilized to a transducer and generate a signal from biorecognition, of which process occurs at the surface of the biosensor, usually [1-10]. For DNA biosensor, single-stranded DNA (ssDNA) or double-stranded DNA (dsDNA) form biorecognition by recognizing target

DNA sequence via hybridization which is immobilized on the surface of biosensor [1-11]. DNA biosensors generate a variety of signals but the electrochemical DNA biosensors are used most-widely. Whole-cell based biosensor is far from cost-effectiveness because the lifetime of a living cell is limited comparing to other receptors. Nevertheless, whole-cell biosensors have many advantages considering its potential application. Most of its advantages are related to the characteristics of the living cells, from which functional information can be directly obtained rather than analytical information [1-12].

Researches for biosensor can be classified into studies enhancing selectivity and sensitivity, roughly. For that, the researchers analyzed signal generation by biorecognition and the biochemical characteristics between analyte and receptor. Likewise, biosensors have been observed and developed in the biochemical perspective but in terms of fabrication of devices and behavior of elements inside the device, the biosensor needs to be investigated, mechanically. Especially, considering that most of the biosensor is surface detection system in which the receptors are immobilized at the surface of the biosensor, analysis for the analyte behavior inside biosensor is necessary in order to enhance the selectivity or sensitivity. In the following section, a description of the sensing mechanism for a surface detection system is provided.

### 1.1.4. Sensing mechanism for a surface detection system

Receptors for the biosensor are commonly immobilized at the surface of the sensor in order to read the signal without

contamination generated by biorecognition. For binding between analyte and receptor, the analyte should be transported to the wall at which the receptor is immobilized as shown in Figure 1-3. When the analyte transported to the wall is captured by the receptor, changes such as mass change or electrical potential change occur and this change generates a signal through the transducer. Thus, as a first step to detect a target, the analyte should be transported towards the surface of the biosensor.

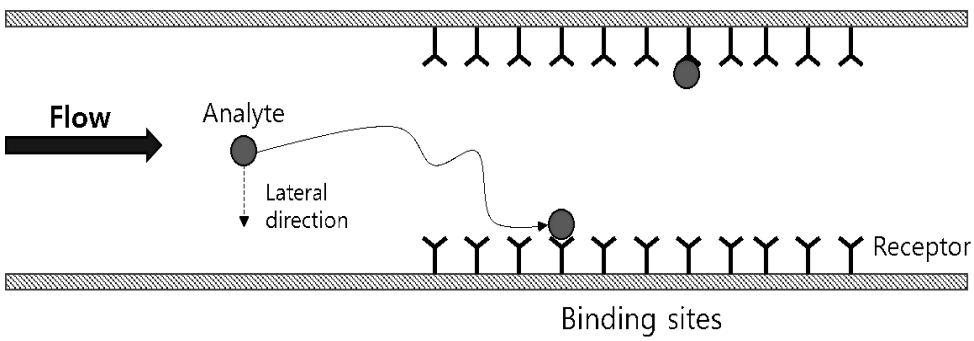


Figure 1-3. The schematic diagram for sensing mechanism of surface detection system biosensor.

In order to enhance the transport of the analyte, there are two options: Generating lateral-direction flow inside the channel, Reducing the distance between analyte and receptor, in other words, increasing the surface-volume ratio.

Especially, in the case of the medical diagnostic field, the biosensor is required to have high sensitivity below ng/ml for early diagnosis [1-13]. Microfluidic channel is adapted to increase surface-volume ratio, still, it is often not enough to satisfy high sensitivity required in the medical diagnostic field. Besides, because the microfluidic channel is commonly adapted, laminar flow is mainly developed inside biosensor considering that most of the diagnostic

devices are performed using capillary flow. The lateral directional flow is difficult to be generated in case of laminar flow in which no vortex occurs. Thus, increasing the surface-to-volume ratio extremely using microbeads or generating lateral flow by mixing structure or external field is introduced. The researches for efficient methods to enhance the sensitivity of biosensor is presented in the following section.

## 1.2. Sensitivity enhancement for a biosensor

### 1.2.1. Improving the surface-to-volume ratio

As mentioned above, increasing the surface-to-volume ratio is a key method to enhance the sensitivity of the biosensor. As one of the simple ways, micro-sized superparamagnetic beads can be used by adding it to the sample solution [1-14]. The surface of the magnetic beads was treated to be carboxylated after the activation process with NHS [N-hydroxysuccinimide] and EDC [1-ethyl-3-(3-di-methyl-aminopropyl) carbodiimide hydrochloride] and coated by receptors. After incubation, the particles which were bound with analytes, in other words, had bio-recognition were collected magnetically and placed onto electrode as shown in Figure 1-4 [1-15].

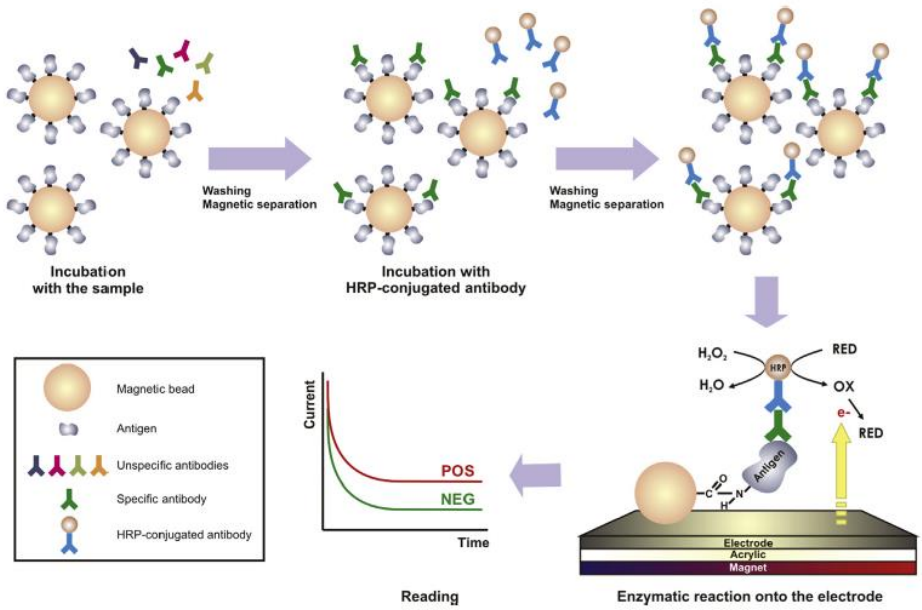


Figure 1-4. Schematic representation of the method for enhancing the sensitivity of biosensor using magnetic beads. Receptors were coated onto the surface of magnetic beads and the particles which have bio-recognition with analytes were collected to electrode [1-15].

Because this method does not require centrifugation device, it is simple and cost-effective compared to conventional pathogen detection methods. Still, this method needs an external field generation device for collecting captured species. Moreover, it requires incubation for binding between analytes and receptors during which nonspecific binding of species to receptor can occur and it may come into a noise of the signal.

Imbedding micro/nano structures onto the surface of biosensor can be an alternative as the method for increasing surface-to-volume ratio. Micro/nano structures can offer a wider surface area for sensing due to its small dimension. For these reasons, nanostructured ZnO has attracted interest, in recent researches for

biosensor [1-16]. As shown in Figure 1-5, nano-sized structures can be formed using the electro-deposition method and the surface-to-volume ratio can be improved [1-17].

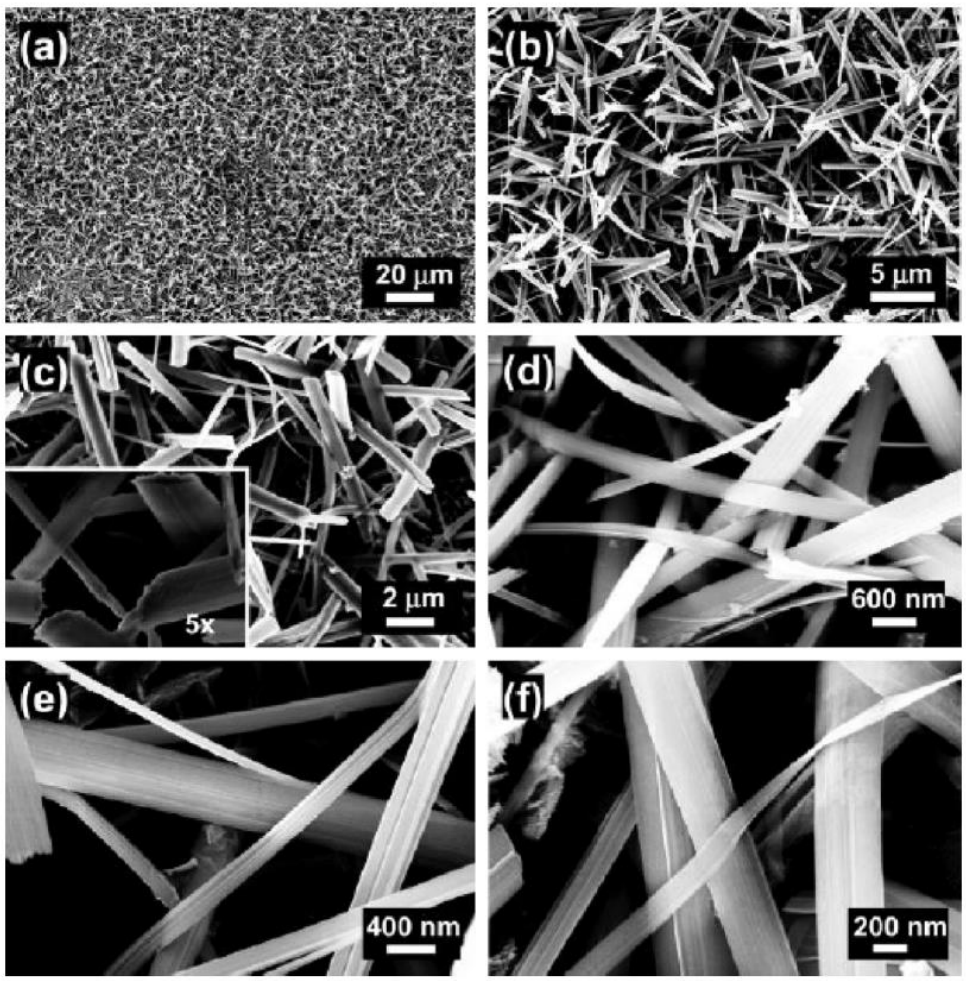


Figure 1-5. SEM images of ZnO nanostructures by the electro-deposition [1-17].

But plenty of costs and treatment time to fabricate nanostructure on the surface of biosensor are taken for this method, which is not suitable considering recent trends requiring not only cost-effectiveness but also portability and simplicity.

### 1.2.2. Lateral-directional movement of the analyte

As another method for enhancing the transport of analyte to receptor, lateral movement towards the surface of biosensor is generated directly through the external field or induced by flow agitation using mixing structures.

A repeating pattern of grooves such as chevron or diagonal stripe pattern induces lateral flow towards sensing surface by making flow agitated as shown in Figure 1-6. With this patterned surface, the intensity of fluorescence was increased until 31 % according to direct assay test using CY-5 fluorescent labeled biotin and 80 μm PDMS channel where avidin was immobilized as a receptor [1-18].

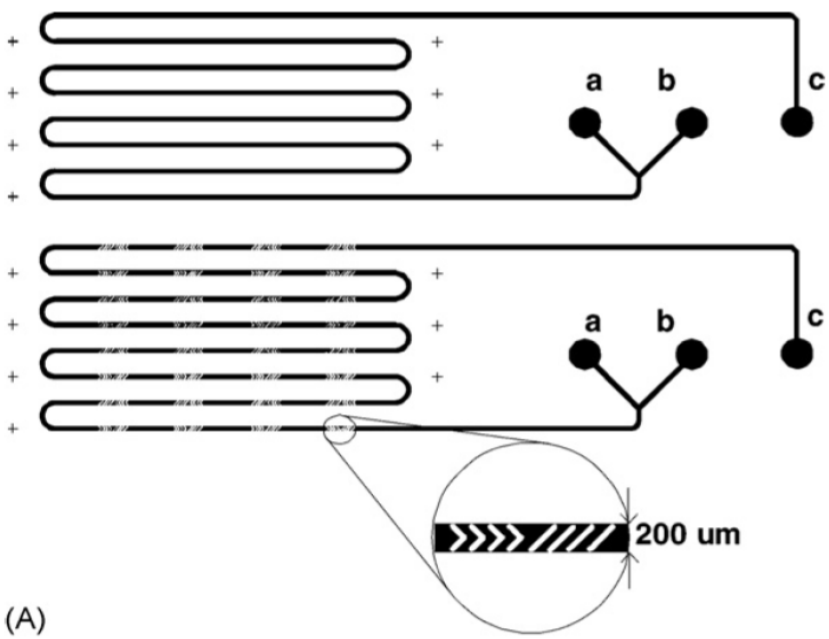


(A)

(B)

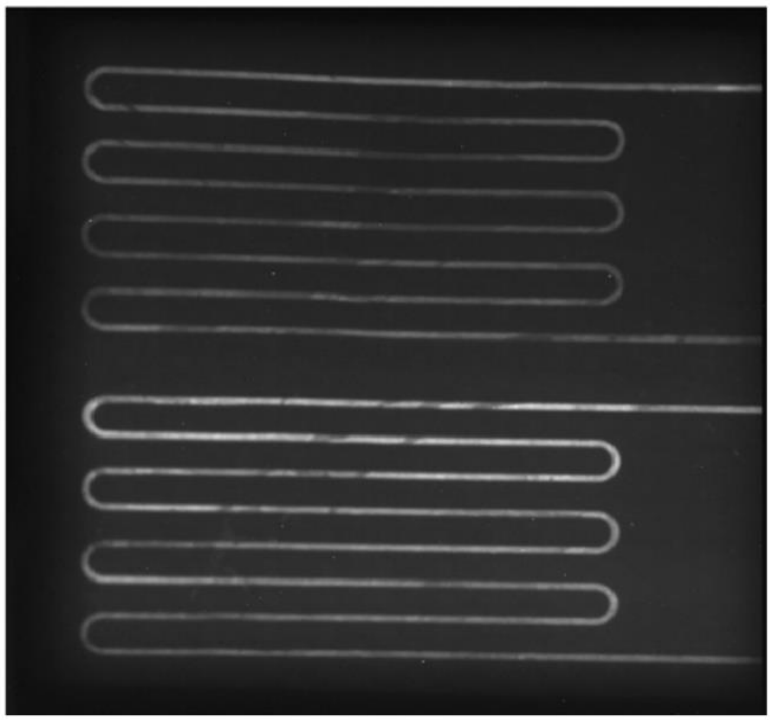

Figure 1-6. (a) Diagram of the microchannel with four chevrons and diagonal stripes patterned surface. (b) Images of PDMS microchannel with mixing structures. The channel was fabricated using softlithograpy [1-18].

Lateral movement of the analyte can be induced directly by exerting an electric field to analyte inside the microchannel. Analytes from the virus to the bacteria, which correspond to the smallest and largest bioparticle, respectively, have a surface charge when they are suspended inside fluid as shown in Figure 1-7. Counterions against the surface charge of bioparticle are crowded adjacent to the bioparticle, which is termed with the Stern layer and the diffuse layer is formed further from the bioparticle [1-19]. These two layers are termed with electric double layers which are formed when two conducting materials meet at their interface [1-20].

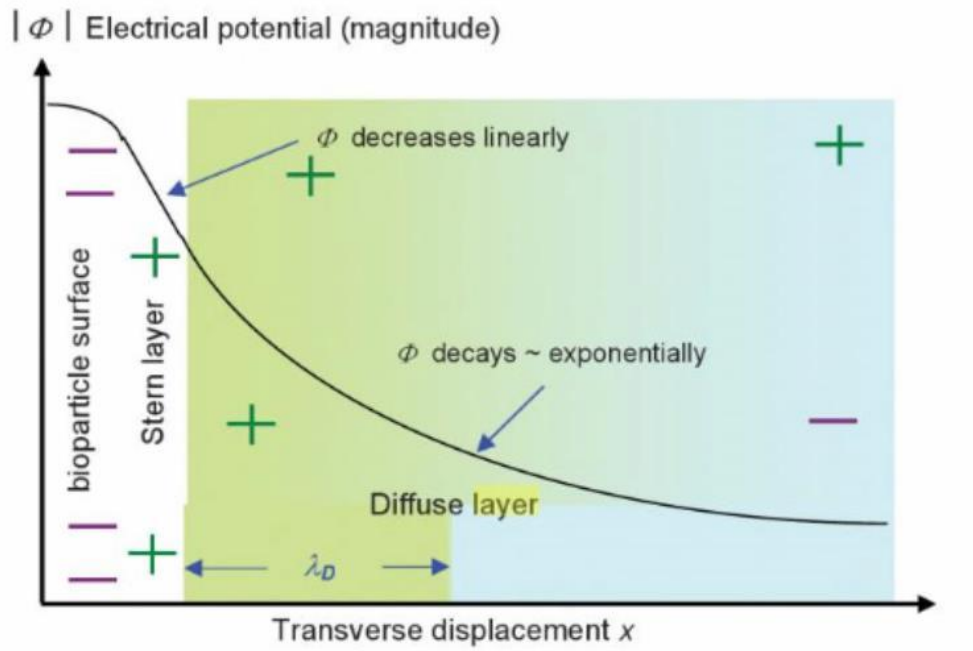


Figure 1-7. Schematics of the electric double layer for the bioparticles [1-19].

Through these electric double layers, analyte has an electric charge on its surface, thus, the analyte can be manipulated by exerting an electric field and have lateral movement when the field is directed perpendicular to the flow direction [1-21].

## 1.3. Purpose of research

In recent years, point-of-care diagnostics have been settled as a critical role in healthcare strategy and there has been tremendous technological progress in point-of-care devices [1-22]. Traditional diagnostic devices were operated only by well-trained professionals who have sophisticated technics [1-23]. But recent researches for the medical diagnostic biosensor have been significantly developed

to such an extent as to require not only low-cost and portability but also accessibility to untrained individuals and instrument-independency. For severe disease, the cost of diagnosis may not be a critical factor to consider but as the coverage of the device is expanded to early diagnosis for diabetes or obesity control, which is considered as mild diseases relatively, demand for the devices with properties indicated above rises in the healthcare industry [1-24]. For easy-to-use and instrument independent biosensor, a method for enhancing the sensitivity without external equipment and high fabrication cost needs to be developed.

Transport of analyte inside the microfluidic channel is usually demonstrated by the diffusion-reaction model which is described in the perspective of concentration [1-25]. However, for the low concentration case in which the continuum hypothesis may not be valid, a transport model based on the dynamics of individual analyte needs to be presented. Furthermore, in the reaction-diffusion model which has Langmuir isotherm assumption, the coefficients of binding kinetics are needed according to each analyte and the stochastic motion of analyte is not considered by which small species such as virus or protein are mainly governed [1-26]. In this study, the transport model by calculating the number of analytes capable of colliding on the wall based on Brownian motion is suggested for optimal design of biosensor.

## 1.4. This thesis

### 1.4.1. Suggestion for a transport model of analytes in a microfluidic channel for a biosensor

In chapter 2, the binding phenomenon was investigated, experimentally, by counting the number of bound biotinylated beads to streptavidin according to the design parameters of the device such as the dimension of the channel or the position of the receptor, and the parameters for the diagnostic process such as the concentration of analytes or flow rate.

For optimal design and estimation of the limit of detection for biosensor, an analyte transport model inside the microfluidic channel is suggested by calculating the number of analytes to collide on the wall based on Brownian motion in chapter 3. The calculated values from a transport model were evaluated by comparing to the experimental results.

### 1.4.2. Cost-effective and instrument-independent method to enhance the sensitivity of a biosensor

In order to enhance the sensitivity of biosensor cost-effectively and instrument-independently, a new method to induce a flow agitation using dummy particles is presented. In chapter 4, the rotational motion of dummy particles was observed from the high-speed camera so that the applicability of the Jeffery model in Poiseuille flow was confirmed and the enhancement of sensitivity using dummy particles was investigated according to dummy particle

volume fraction, flow rate and size of dummy particle. Lastly, an analysis for the enhancement of sensitivity using dummy particles was performed, numerically, by setting binding zone, in which the analyte is bound to the receptor, immediately.

## Reference

[1-1] Maniya, N. H.; Srivastava, D. N., Fabrication of porous silicon based label-free optical biosensor for heat shock protein 70 detection. *Materials Science in Semiconductor Processing* 2020, *115*, 105126.

[1-2] Conroy, P. J.; Hearty, S.; Leonard, P.; O' Kennedy, R. J. In *Antibody production, design and use for biosensor-based applications*, Seminars in cell & developmental biology, Elsevier: 2009; pp 10-26.

[1-3] Bhalla, N.; Jolly, P.; Formisano, N.; Estrela, P., Introduction to biosensors. *Essays Biochem* 2016, *60* (1), 1-8.

[1-4] Justino, C. I.; Rocha-Santos, T. A.; Duarte, A. C., Review of analytical figures of merit of sensors and biosensors in clinical applications. *TrAC Trends in Analytical Chemistry* 2010, *29* (10), 1172-1183.

[1-5] Alhadrami, H. A., Biosensors: Classifications, medical applications, and future prospective. *Biotechnology and applied biochemistry* 2018, *65* (3), 497-508.

[1-6] Reder-Christ, K.; Bendas, G., Biosensor applications in the field of antibiotic research—A review of recent developments. *Sensors* 2011, *11* (10), 9450-9466.

[1-7] Yoo, S. M.; Lee, S. Y., Optical biosensors for the detection of pathogenic microorganisms. *Trends in biotechnology* 2016, *34* (1), 7-25.

[1-8] Pohanka, M.; Skládal, P., Electrochemical biosensors-principles and applications. *Journal of Applied Biomedicine (De Gruyter Open)* 2008, *6* (2).

[1-9] Paddle, B. M., Biosensors for chemical and biological agents of defence interest. *Biosensors and Bioelectronics* 1996, *11* (11), 1079-1113.

[1-10] Rogers, K. R., Principles of affinity-based biosensors. *Molecular biotechnology* 2000, *14* (2), 109-129.

[1-11] Kerman, K.; Kobayashi, M.; Tamiya, E., Recent trends in electrochemical DNA biosensor technology. *Measurement Science and Technology* 2003, *15* (2), R1.

[1-12] Bousse, L., Whole cell biosensors. *Sensors and Actuators B: Chemical* 1996, *34* (1-3), 270-275.

[1-13] Mascini, M., Biosensors for medical applications. *Sensors and Actuators B: Chemical* 1992, *6* (1-3), 79-82.

[1-14] Rife, J.; Miller, M.; Sheehan, P.; Tamanaha, C.; Tondra, M.; Whitman, L., Design and performance of GMR sensors for the detection of magnetic microbeads in biosensors. *Sensors and Actuators A: Physical* 2003, *107* (3), 209-218.

[1-15] Cortina, M. E.; Melli, L. J.; Roberti, M.; Mass, M.; Longinotti, G.; Tropea, S.; Lloret, P.; Serantes, D. A. R.; Salomón, F.; Lloret, M., Electrochemical magnetic microbeads-based biosensor for point-of-care serodiagnosis of infectious diseases. *Biosensors and Bioelectronics* 2016, *80*, 24-33.

[1-16] Morris, J. E.; Iniewski, K., Nanoelectronic device applications handbook. American Society of Mechanical Engineers Digital Collection: 2013.

[1-17] Arya, S. K.; Saha, S.; Ramirez-Vick, J. E.; Gupta, V.; Bhansali, S.; Singh, S. P., Recent advances in ZnO nanostructures and thin films for biosensor applications. *Analytica chimica acta* 2012, *737*, 1-21.

[1-18] Golden, J. P.; Floyd-Smith, T. M.; Mott, D. R.; Ligler, F. S., Target delivery in a microfluidic immunosensor. *Biosensors and Bioelectronics* 2007, *22* (11), 2763-2767.

[1-19] Bakewell, D., *Micro-and nano-transport of biomolecules*. BookBoon: 2008.

[1-20] Schmickler, W., Electrochemical Theory: Double Layer. 2014.

[1-21] Zourob, M.; Elwary, S.; Turner, A. P., *Principles of bacterial detection: biosensors, recognition receptors and microsystems*. Springer Science & Business Media: 2008.

[1-22] Zarei, M., Portable biosensing devices for point-of-care diagnostics: Recent developments and applications. *TrAC Trends in Analytical Chemistry* 2017, *91*, 26-41.

[1-23] Narayan, R. J., *Medical Biosensors for Point of Care (POC) Applications*. Woodhead Publishing: 2016.

[1-24] Yoo, E.-H.; Lee, S.-Y., Glucose biosensors: an overview of use in clinical practice. *Sensors* 2010, *10* (5), 4558-4576.

[1-25] Jomeh, S.; Hoorfar, M., Numerical modeling of mass transport in microfluidic biomolecule-capturing devices equipped with reactive surfaces. *Chemical Engineering Journal* 2010, *165* (2), 668-677.

[1-26] Gervais, T.; Jensen, K. F., Mass transport and surface reactions in microfluidic systems. *Chemical engineering science* 2006, *61* (4), 1102-1121.

# Chapter 2. Transport and the binding phenomenon of analytes in microfluidic channel

This chapter is based on:

Choi, S.; Lee, W.I.; Lee, G.H.; Yoo, Y.-E. Analysis of the Binding of Analyte-Receptor in a Micro-Fluidic Channel for a Biosensor based on Brownian Motion. *Micromachines* 2020, 11, 570.

## 2.1. Overview

In this chapter, in order to examine the transport of analyte towards wall depending on the detection conditions such as the concentration of the sample, flow rate, and the receptor-analyte binding measurement position, the number of bound analytes was counted while the sample solution containing analytes flowed through a microfluidic channel. Target analyte and receptor for experiments need to have high affinity so that binding of the analyte close to the receptor can be maximized. Thus, in terms of the model receptor, streptavidin was immobilized on the micro-channel surface and as for the analyte, fluorescent biotinylated Polystyrene beads (FluoSpheres™ Biotin-Labeled Microspheres, diameter: 200 nm) was used which shows excellent binding properties with streptavidin. The binding between streptavidin-biotin was confirmed by measuring the fluorescence of biotinylated polystyrene beads. In the following section, the properties of streptavidin and biotin are explained, and experimental methods are followed in section 2.3 and section 2.4. The results and discussion are presented in the last section.

## 2.2. Streptavidin-biotin binding

Streptavidin is a protein that has a high affinity for biotin and its size is estimated as 4 nm [2-2]. The dissociation constant is approximately ~$10^{-14}$ mol/L and the streptavidin-biotin bonding is one of the strongest non-covalent bonding [2-3]. The binding between streptavidin and biotin is independent on temperature or ionic strength but the stability is affected by pH as shown in Figure 2-1 [2-4]. Thus the pH value of the solution used in all of the experiments is controlled carefully at pH 7.

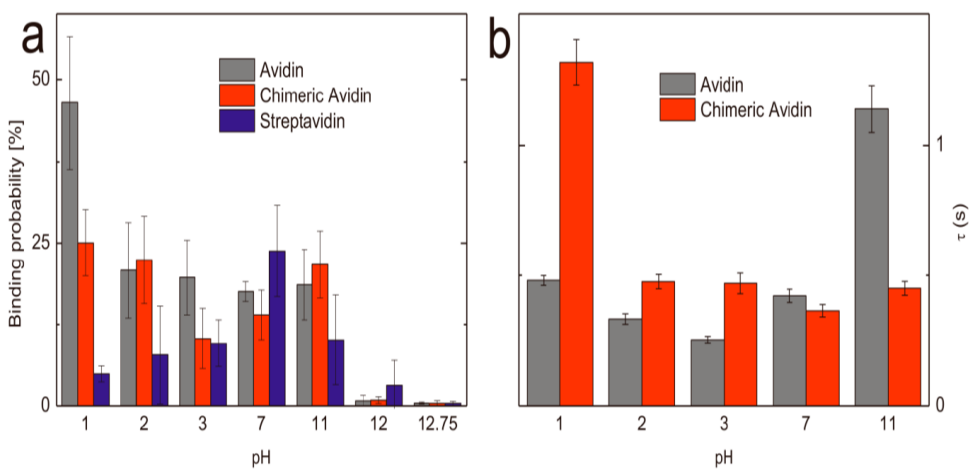


Figure 2-1. (a) Binding probability of avidin, chimeric avidin, and streptavidin at different pH. (b) A complex lifetime of avidin and chimeric avidin bound with biotin [2-4].

## 2.3. Microfluidic channel and surface modification

As shown in Figure 2-2, a micro-fluidic channel was designed to be 100 μm in depth (H = 100 μm) and 5 mm in width (W = 5 mm) to reduce the side wall effect of the channel on the flow. The length

of the channel was set to 70 mm. A transparent microfluidic channel substrate was injection molded using PMMA (Polymethyl methacrylate) to observe the behavior of the particles and fluorescent image of the polystyrene (PS) particles bound to the streptavidin.

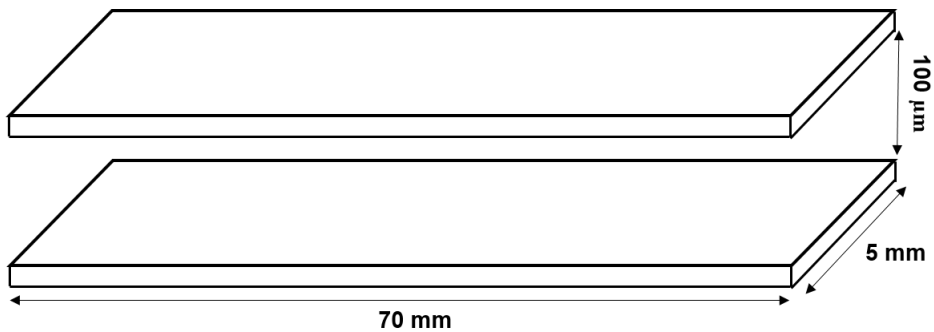


Figure 2-2. The dimension of a microfluidic channel. The top and bottom substrate of the channel were manufactured using injection molding and the channel was fabricated with 100 μm double-sided film.

For the biotinylated beads-streptavidin binding, streptavidin is required to be immobilized previously on the PMMA microchannel surface, which consists of several processes as follows. After sonication in isopropanol (IPA) for 15 min, PMMA substrates were washed three times with IPA and DI water, in turn. The surface of the micro-channel was carboxylated by exposure to UV light for 30 min for effective streptavidin coating [2-5]. Streptavidin was immobilized onto the PMMA surface by dipping in the coating solution, a mixture of 50 μL of streptavidin, 25 mg of EDC (1-ethyl-3-(3-dimethylamino propyl) carbodiimide) reagent, and 5 mL of MES buffer. EDC was used for facilitating the binding of the amino part of streptavidin with carboxyl groups on the PMMA surface. After

incubation for 2h 30 min, the PMMA substrates were washed and dried with nitrogen gas [2-6].

Immobilization of streptavidin onto the PMMA surface was confirmed by investigating N/C ratio through X-ray photoelectron spectroscopy (XPS) as shown in Figure 2-3. N/C ratio for carboxylated and chemisorbed PMMA surface shows the largest value (approximately 0.05).

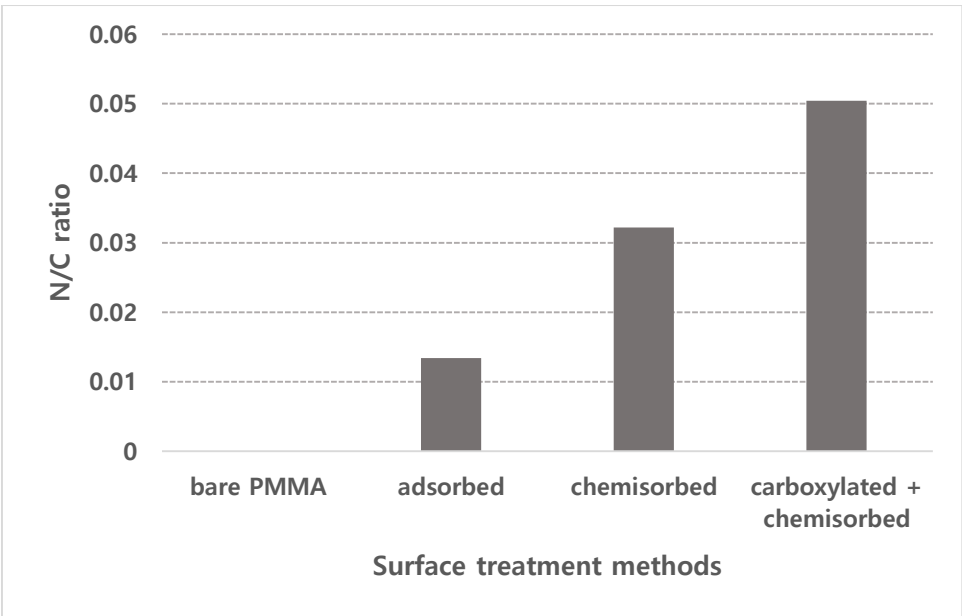


Figure 2-3. N/C ratio according to different surface treatment methods through XPS. “adsorbed” indicates the case only with the streptavidin incubation process onto bare PMMA and the “chemisorbed” method contains activation process using EDC. “carboxylated + chemisorbed” corresponds the case containing carboxylation, activation, and incubation process.

The model of the instrument for XPS was Axis Supra (Kratos, U.K.) and the spectroscopy conditions were shown in Table 2-1.

Table 2-1. Conditions for XPS

| X-ray source | | Monochromatic Al-K $\alpha$ (15 kV, 300 W, 400 $\mu$m) |
|---|---|---|
| Wide scan | Pass energy | 80 eV |
| | Step size | 1.0 eV |
| Narrow scan | Pass energy | 20 eV |
| | Step size | 0.1 eV |
| Flood gun | On | |
| Ion etching gun | Off | |

Using the results of XPS, the surface coverage of streptavidin is calculated as below [2-7].

$$\text{Surface coverage} = \frac{Nitrogen\ (XPS)}{Carbon\ (XPS)} \times \frac{Carbon\ (Protein)}{Nitrogen\ (Protein)} = 0.18$$

## 2.4. Investigation for bound particles

The experiments were performed by flowing the sample solution during each detection time. After injecting the sample solution containing biotinylated beads, the microfluidic channel was washed three times by 10 mL of deionized water for each washing in order to prevent non-intended adsorption of beads. The flow rate of DI water for washing was 10 mL/h and non-specific binding of beads was investigated through the fluorescence microscope. Because the experiments were performed under flowing condition and the bead solution used for the experiments contained non-ionic surfactant, Tween 20, none of the beads were bound to bare PMMA after washing.

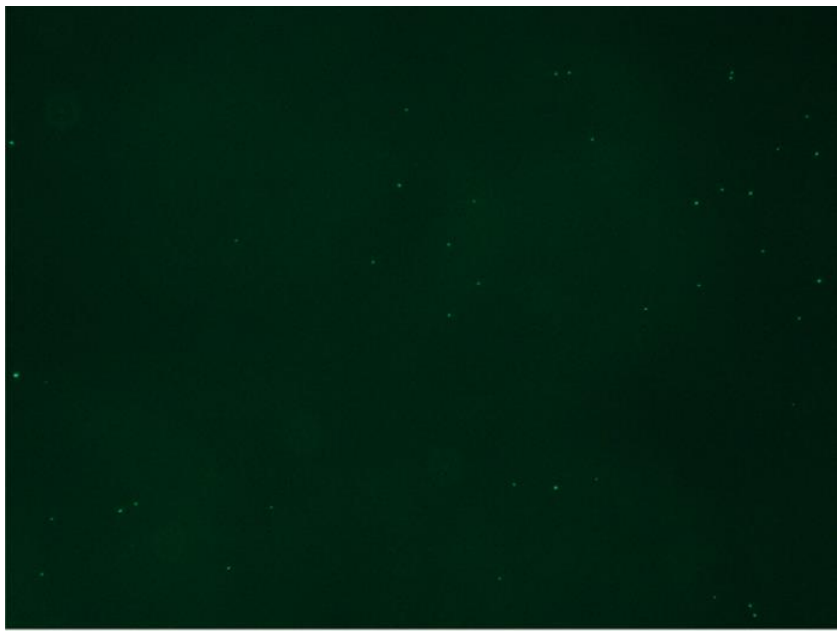

(a)

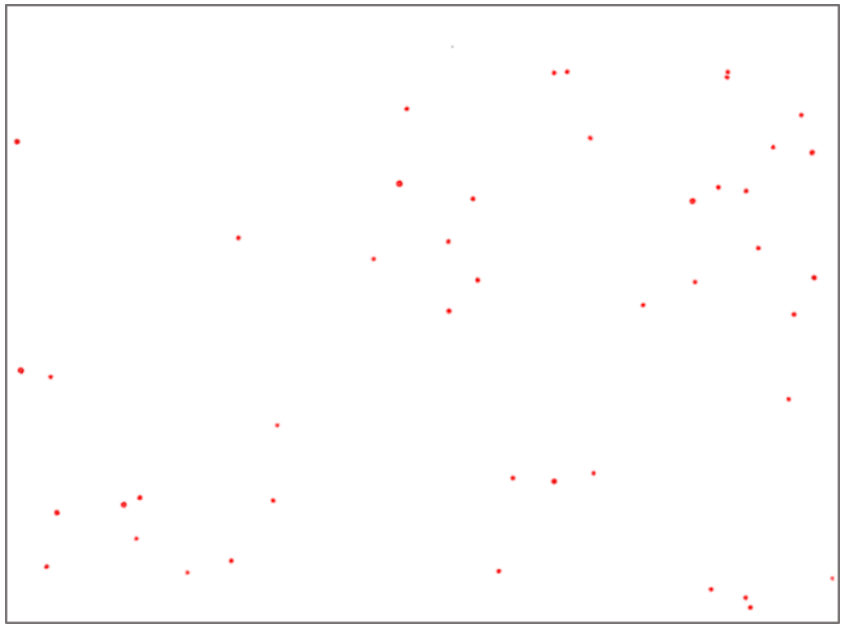

(b)

Figure 2-4. Image for fluorescent biotinylated PS bead bound to streptavidin on the surface of the micro-channel (a) from fluorescent microscopy (b) after image processing for counting the bound beads.

Images of the biotinylated beads bound to a specific area ($W_1$ = 1362 μm, $W_2$ = 1021 μm) of microfluidic channel surface were obtained with a fluorescence microscope. As shown in Figure 2−4, by setting a binary threshold the noise was removed and through image processing, the fluorescent intensity by the bound beads was flattened. Finally, the number of particles bound in the microscopic area shown in Figure 2−5 were counted discretely using a finding circles function.

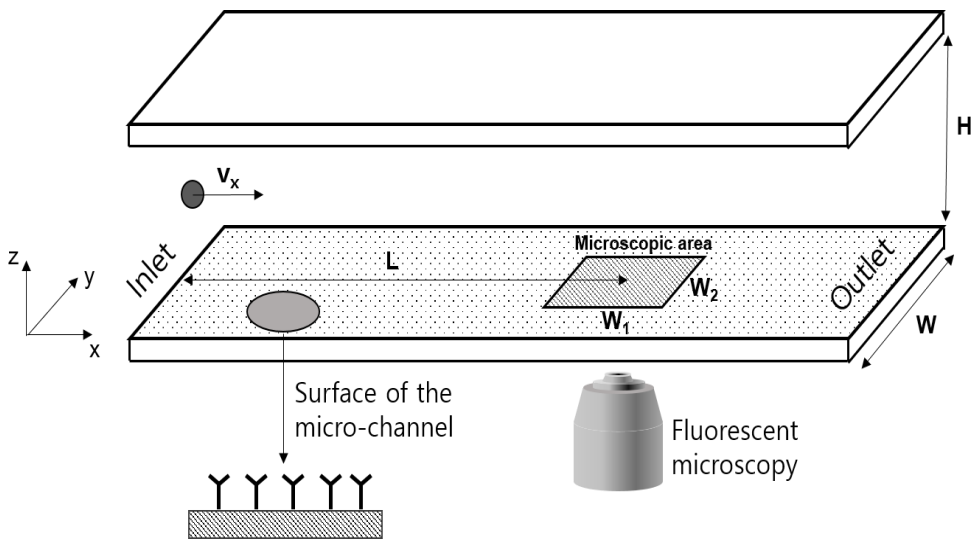


Figure 2−5. Configuration of the experiments.

The experiments were repeated five times for each condition shown in Table 2−2 below. The conditions for flow rate were 0.3 mL · $h^{-1}$, 1.2 mL · $h^{-1}$, and 2.4 mL · $h^{-1}$. In the case of 1.2 mL · $h^{-1}$, the average velocity of the flow ($\overline{v_x}$) is equivalent to about 0.67 mm · $s^{-1}$ which can be assumed to be fully laminar flow. Besides, the bound beads were observed at three different observation positions to investigate the effect of flow distance and optimize the scanning area. The observation positions were 10 mm, 35 mm, and 60 mm from the inlet, respectively.

Table 2-2. Experimental conditions.

| Number Density (n) | Flow Rate | Observation Position (L) |
|---|---|---|
| $1.93 \times 10^{15}\ m^{-3}$ | 1.2 mL · $h^{-1}$ | 35 mm |
| $1.93 \times 10^{14}\ m^{-3}$ | 1.2 mL · $h^{-1}$ | 35 mm |
| $1.93 \times 10^{13}\ m^{-3}$ | 1.2 mL · $h^{-1}$ | 35 mm |
| $1.93 \times 10^{12}\ m^{-3}$ | 1.2 mL · $h^{-1}$ | 35 mm |
| $1.93 \times 10^{14}\ m^{-3}$ | 0.3 mL · $h^{-1}$ | 35 mm |
| $1.93 \times 10^{14}\ m^{-3}$ | 2.4 mL · $h^{-1}$ | 35 mm |
| $1.93 \times 10^{14}\ m^{-3}$ | 1.2 mL · $h^{-1}$ | 10 mm |
| $1.93 \times 10^{14}\ m^{-3}$ | 1.2 mL · $h^{-1}$ | 60 mm |

## 2.5. The number of bound particles

Figure 2-6 shows the results of measuring the number of bound particles according to the detection time under the conditions of number density n = $1.93 \times 10^{15}\ m^{-3}$, flow rate = 1.2 mL · $h^{-1}$, and observation position = 35 mm. The number of bound particles increased linearly over time.

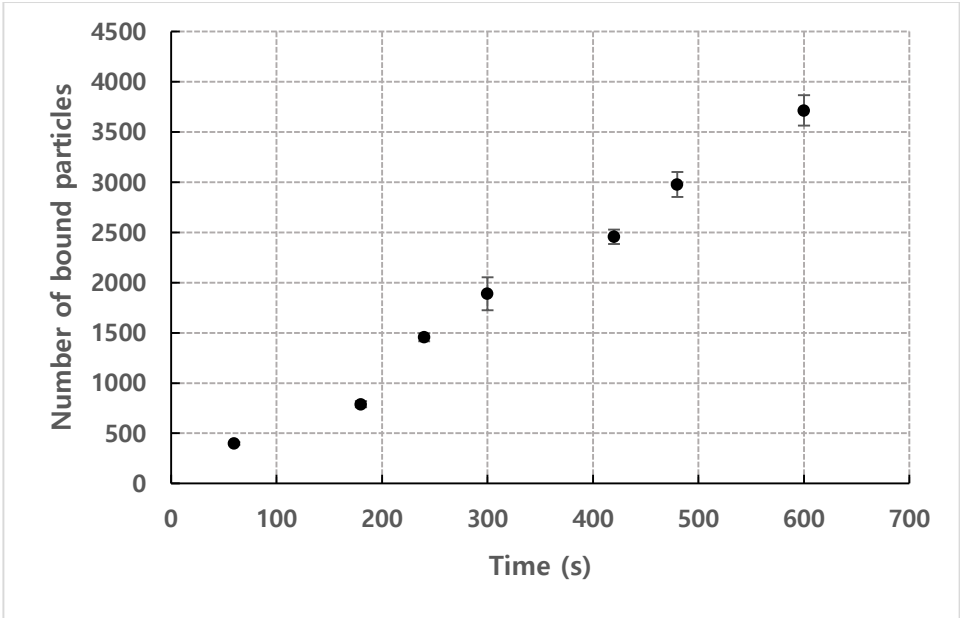


Figure 2-6. Result of measuring the number of bound particles according to the detection time (n = $1.93 \times 10^{15}$ $m^{-3}$, flow rate = 1.2 mL · $h^{-1}$, observation position = 35 mm).

### 2.5.1. Concentration effect

Under the conditions of flow rate = 1.2 mL · $h^{-1}$ and observation position = 35 mm, the number of bound particles according to the detection time for each concentration was normalized by number density n and it is shown in Figure 2-7.

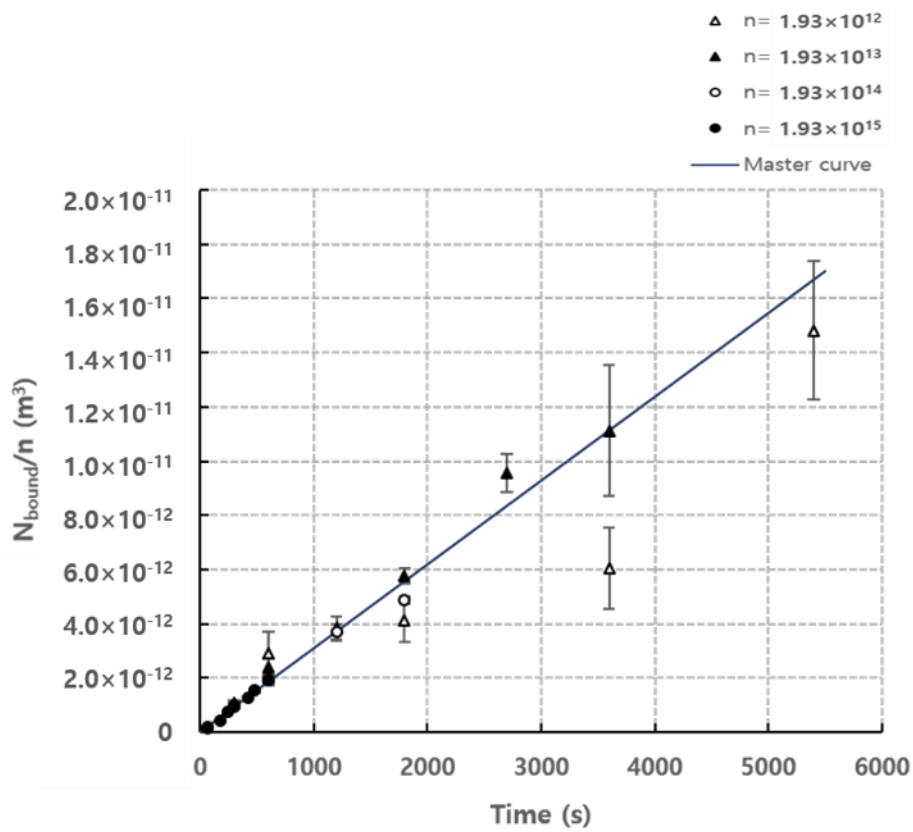


Figure 2-7. Normalized $N_{bound}$ according to the time for each concentration (Normalized by number density n), flow rate = 1.2 mL · $h^{-1}$, observation position = 35 mm. The master curve was fitted using the least square method ($R^2 = 0.90$).

The number of bound particles normalized by number density has a similar trend for each concentration, so the concentration of analyte affects only the total number of analytes injected into microchannel and there is not any mechanism transition for the binding according to concentration.

As shown in the graph, the normalized values approximate to a single linear curve, which was estimated by the least square method, and the coefficient of determination was 0.90. For the lowest concentration (number density n= $1.93 \times 10^{12}$ $m^{-3}$), it shows a

relatively large deviation according to time, because the size of the sample was small. But considering the results through the whole time on average, it fits the master curve with the deterministic coefficient was 0.8 for the lowest concentration case.

### 2.5.2. Flow rate effect

Figure 2-8a shows the result of the number of bound particles for each flow rate over time under the conditions of n = $1.93 \times 10^{14}$ $m^{-3}$ and observation position = 35 mm. Figure 2-8b shows the number of bound particles according to the quantity of the sample solution in order to investigate the binding efficiency depending on the flow rate of the sample. 0.1 mL of the sample contains approximately $1.93 \times 10^{7}$ analytes considering that the number density of the sample was $1.93 \times 10^{14}$ $m^{-3}$. The traveling time for particles to be bound to the microscopic area by Brownian motion increases as the flow rate decreases, so the binding efficiency increases as the flow rate decreases, as shown in Figure 2-8b. Considering these results, lower flow rate is better to reduce the waste of samples.

As shown in Figure 2-9, the proportionality was far below 1 so that the increased number of bound particles was much less compared to that of total injected analytes by increasing flow rate.

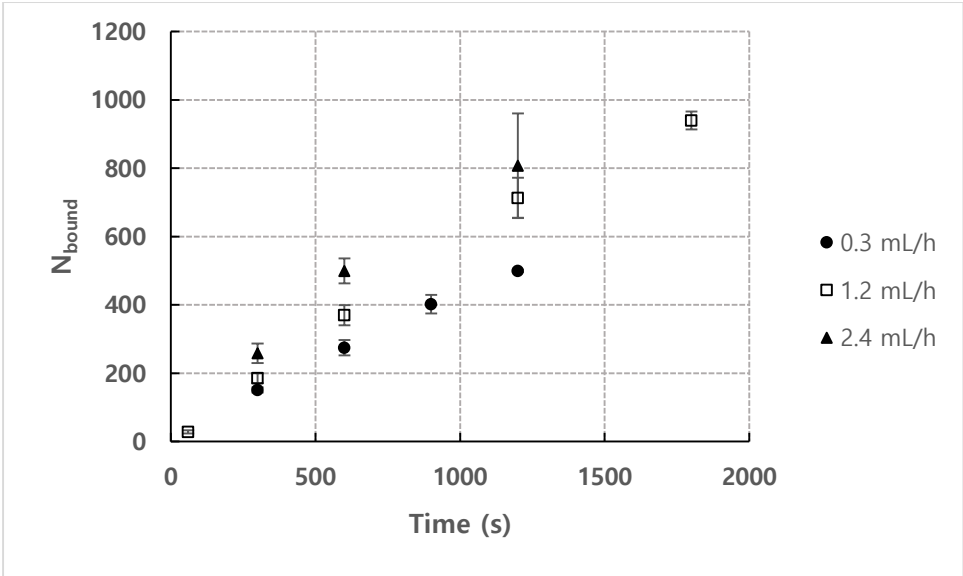


(a)

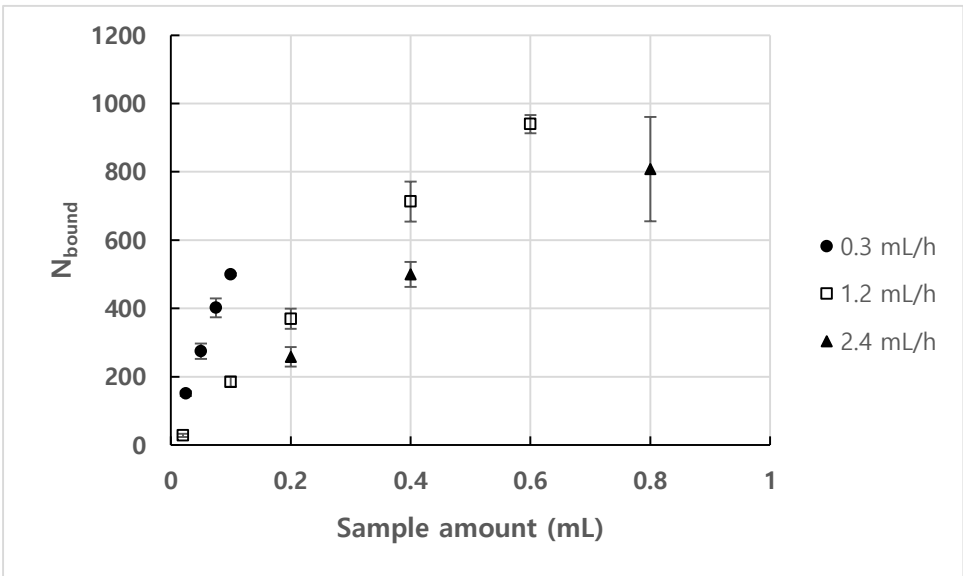


(b)

Figure 2-8. Number of bound particles under different flow rate condition depending on (a) time, (b) sample amount. (n = $1.93 \times 10^{14}$ $m^{-3}$, observation position = 35 mm).

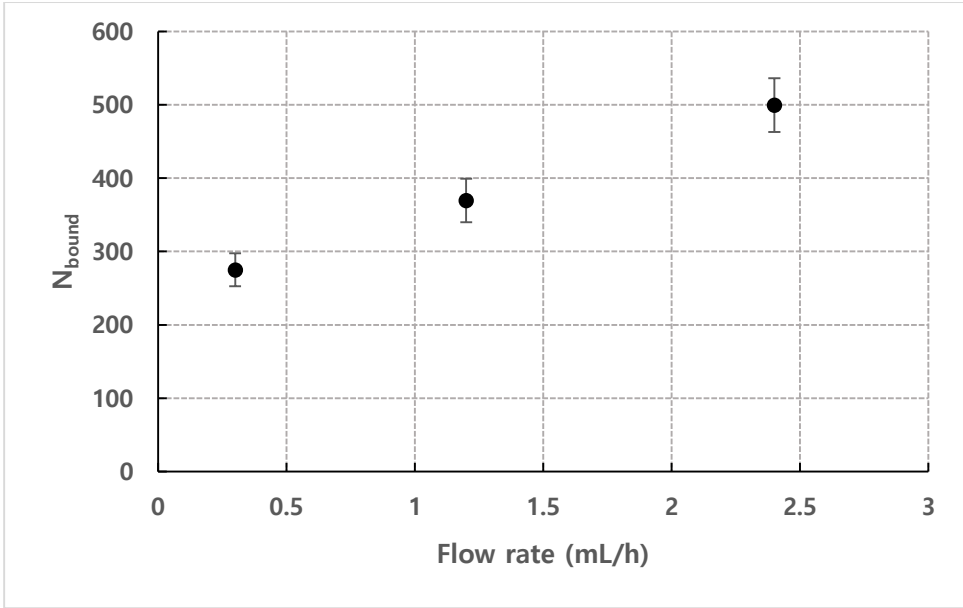


(a)

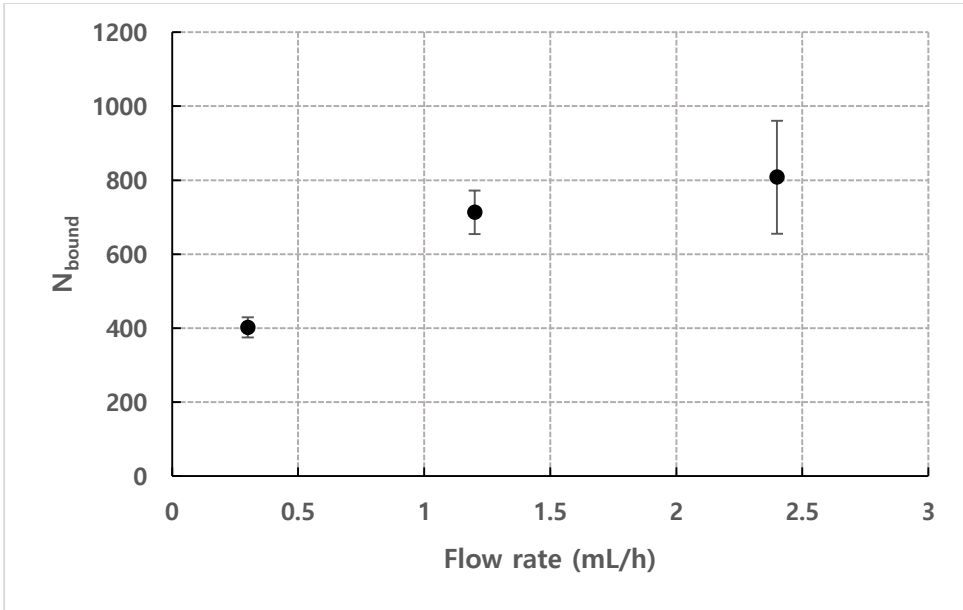


(b)

Figure 2-9. The number of bound particles according to flow rate. Detection time was fixed at (a) 600 s, (b) 1200 s. (n = $1.93 \times 10^{14}$ $m^{-3}$, observation position = 35 mm).

### 2.5.3. Effect of observation position from the inlet

Figure 2-10 shows the result of the number of bound particles depending on the observation positions under the conditions of n = $1.93 \times 10^{14}$ $m^{-3}$, $\tau$ = 1200 s, and flow rate = 1.2 mL · $h^{-1}$. The number of bound particles decreases exponentially as the observation position is placed far from the inlet, therefore, the possibility to find the bound analytes increases as the scanning area is close to the inlet.

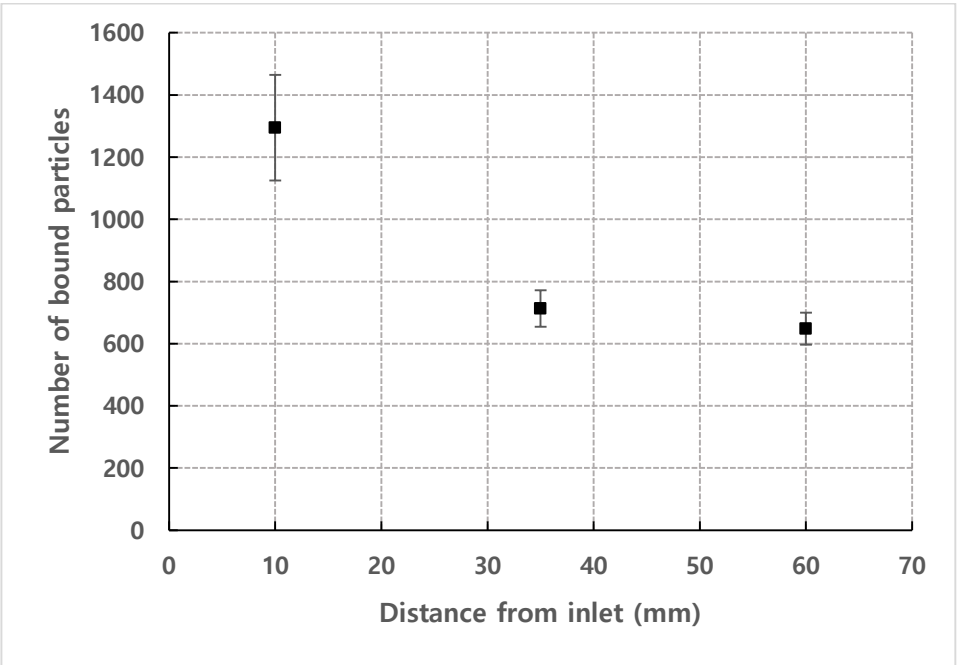


Figure 2-10. Number of bound particles depending on the distance of the observation position from inlet (n = $1.93 \times 10^{14}$ $m^{-3}$, $\tau$ = 1200 s, Flow late = 1.2 mL · $h^{-1}$).

### 2.5.4. Effect of ionic strength and surfactant

In order to investigate the effect of ionic strength, 0.05M, 0,1M, 0.5M NaCl was added into the sample solution and the number of

bound particles is shown in Figure 2-11 under the condition n = $1.93 \times 10^{14}\ m^{-3}$, Flow late = 1.2 $mL \cdot h^{-1}$. Debye length for the solution containing colloidal suspension is given below [2-8].

$$\kappa^{-1} = \sqrt{\frac{\varepsilon_r \varepsilon_0 k_B T}{2 N_A e^2 I}} \qquad (2-1)$$

where I is the ionic strength of the electrolyte ($mole/m^3$), $\varepsilon_0$ is the permittivity of free space, $\varepsilon_r$ is the dielectric constant, $k_B$ is the Boltzmann constant, T is the absolute temperature in kelvins, $N_A$ is the Avogadro number. e is the elementary charge.

Using Equation (2-1), zeta potential and Debye length corresponding to each ionic strength can be calculated as shown in Table 2-3.

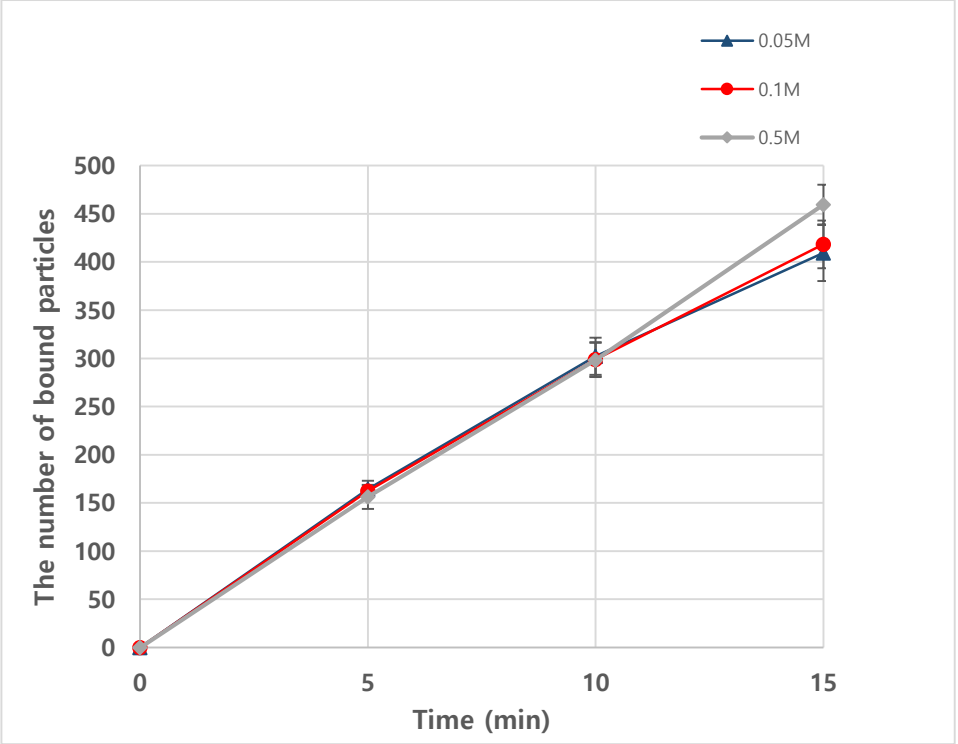


Figure 2-11. The number of bound particles depending on time containing sodium chloride. (n = $1.93 \times 10^{14}$ $m^{-3}$, Flow late = 1.2 $mL \cdot h^{-1}$)

Table 2-3. Zeta potential and Debye length according to the ionic strength of the solution.

| Ionic strength | 0.05 M | 0.1 M | 0.5 M |
|---|---|---|---|
| Zeta potential | −22.6 mV | −20.3 mV | −15.9mV |
| Debye length | 1.36 nm | 1 nm | 0.5 nm |

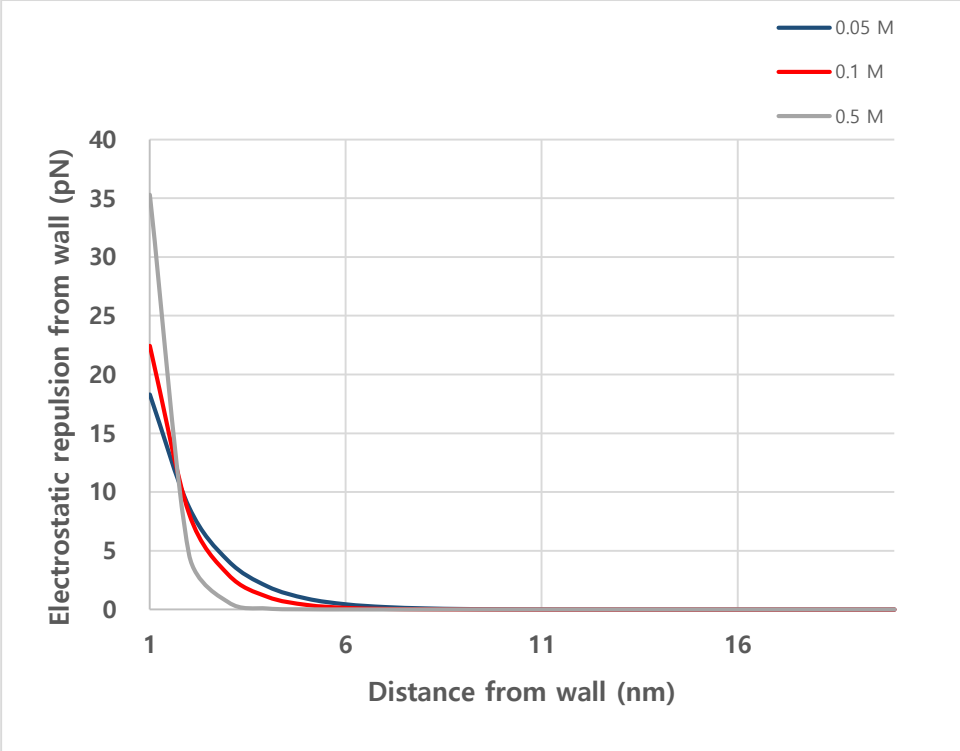


Figure 2-12. Electrostatic repulsion force by PMMA surface depending on the distance from the wall.

Using the values in Table 2-3, electrostatic force can be calculated and it is shown in Figure 2-12. The number of bound particles does not have an obvious trend according to ionic strength although the electrostatic force according to ionic strength is distinguishable, relatively. Meanwhile, it is confirmed that the bonding between streptavidin and biotin is not affected by ionic strength.

As mentioned above, streptavidin has a high affinity for biotin, thus, the bonding between streptavidin and biotin is known to be not affected by the addition of surfactants such as Tween 20 so that Tween 20 is mainly used to exclude non-specific binding phenomenon. But, in this study, the binding between streptavidin and biotinylated bead tremendously decreased with a small portion of

Sodium Dodecyl Sulfate (SDS), as shown in Figure 2-13.

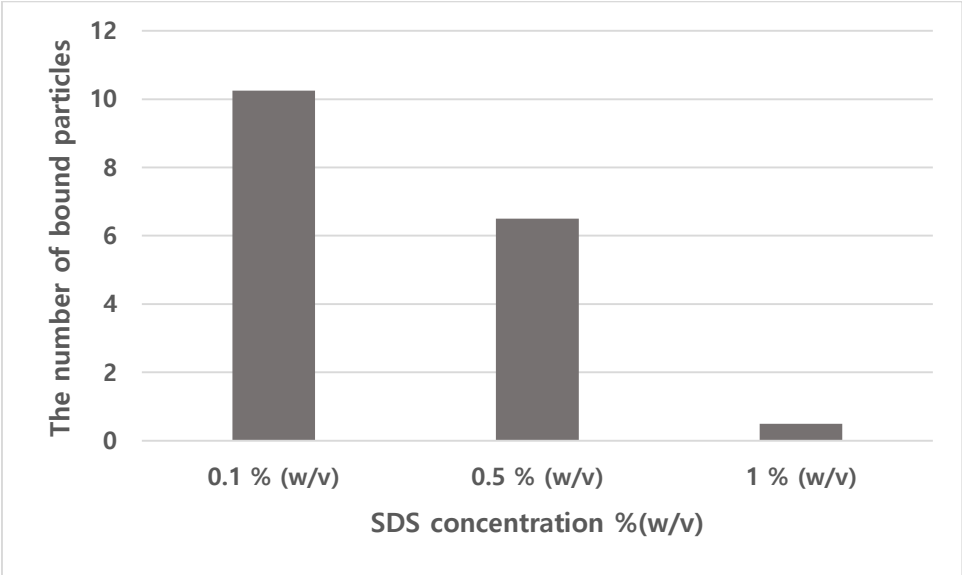


Figure 2-13. The number of bound particles according to SDS concentration. (n = $1.93 \times 10^{14}$ $m^{-3}$, $\tau$ = 600 s, Flow late = 1.2 $mL \cdot h^{-1}$)

## Reference

[2-1] Choi, S.; Lee, W.I.; Lee, G.H.; Yoo, Y.-E. Analysis of the Binding of Analyte-Receptor in a Micro-Fluidic Channel for a Biosensor based on Brownian Motion. *Micromachines* 2020, 11, 570.

[2-2] Shu, W.; Laue, E. D.; Seshia, A. A., Investigation of biotin-streptavidin binding interactions using microcantilever sensors. *Biosensors and bioelectronics* 2007, *22* (9-10), 2003-2009.

[2-3] Green, N. M., Avidin. In *Advances in protein chemistry*, Elsevier: 1975; Vol. 29, pp 85-133.

[2-4] Köhler, M.; Karner, A.; Leitner, M.; Hytönen, V. P.; Kulomaa, M.; Hinterdorfer, P.; Ebner, A., pH-dependent deformations of the energy landscape of avidin-like proteins investigated by single molecule force spectroscopy. *Molecules* 2014, *19* (8), 12531-12546.

[2-5] Wei, S.; Vaidya, B.; Patel, A. B.; Soper, S. A.; McCarley, R. L., Photochemically patterned poly (methyl methacrylate) surfaces used in the fabrication of microanalytical devices. *The Journal of Physical Chemistry B* 2005, *109* (35), 16988-16996.

[2-6] Vesel, A.; Elersic, K.; Mozetic, M., Immobilization of protein streptavidin to the surface of PMMA polymer. *Vacuum* 2012, *86* (6), 773-775.

[2-7] Manakhov, A.; Permyakova, E.; Ershov, S.; Miroshnichenko, S.; Pykhtina, M.; Beklemishev, A.; Kovalskii, A.; Solovieva, A., XPS Modeling of Immobilized Recombinant Angiogenin and Apoliprotein A1 on Biodegradable Nanofibers.

*Nanomaterials* 2020, *10* (5), 879.

[2-8] Russel, W. B.; Russel, W.; Saville, D. A.; Schowalter, W. R., *Colloidal dispersions*. Cambridge university press: 1991.

# Chapter 3. Transport model of analytes in a microfluidic channel for biosensor

This chapter is based on:

Choi, S.; Lee, W.I.; Lee, G.H.; Yoo, Y.-E. Analysis of the Binding of Analyte-Receptor in a Micro-Fluidic Channel for a Biosensor based on Brownian Motion. *Micromachines* 2020, 11, 570.

## 3.1. Overview

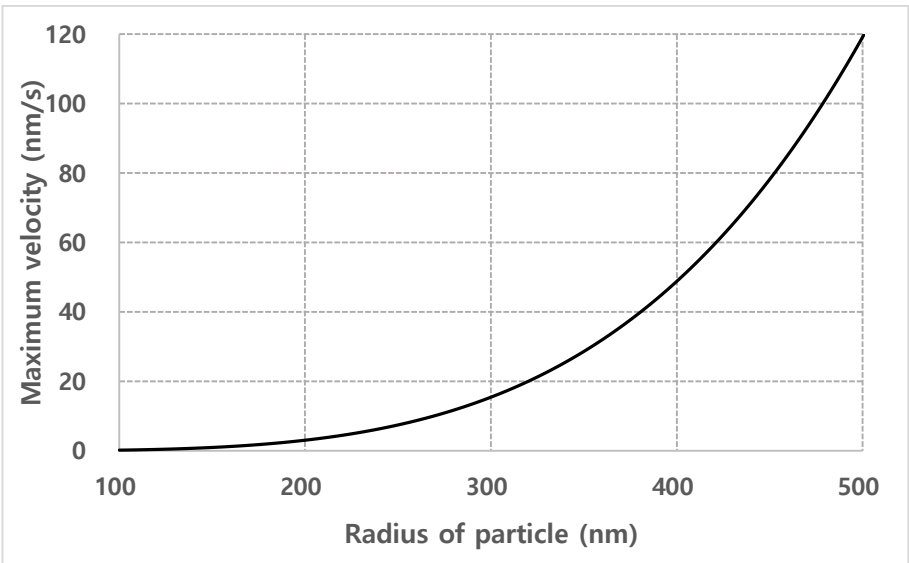


(a)

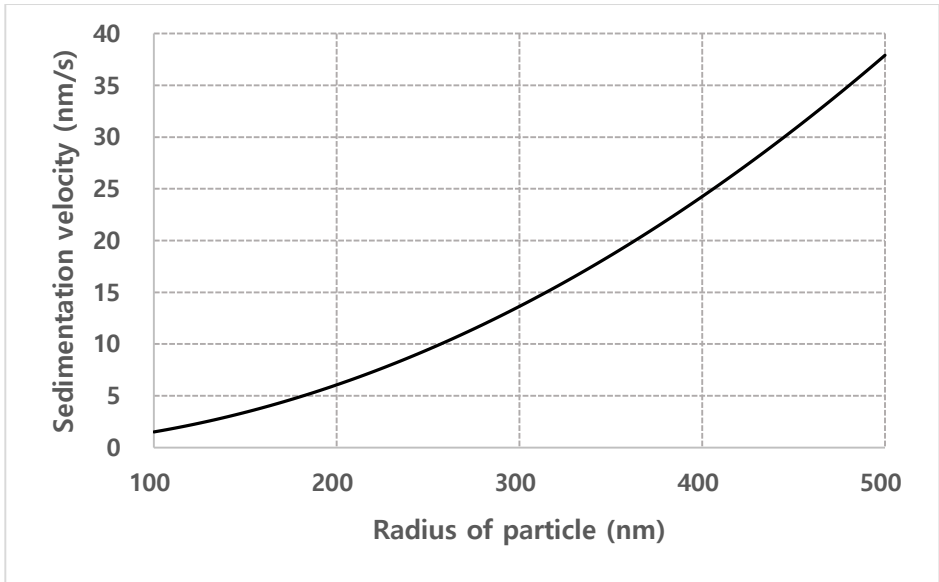


(b)

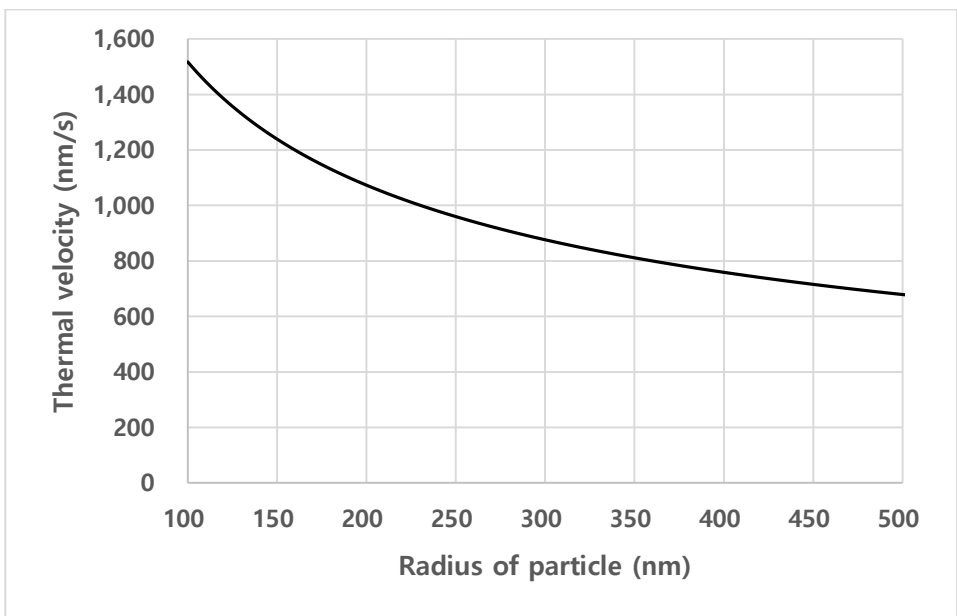


(c)

Figure 3-1. (a) Maximum velocity induced by lift force according to the radius of the particle, (b) Sedimentation velocity according to the radius of the particle, (c) Thermal velocity depending on the radius of the particle.

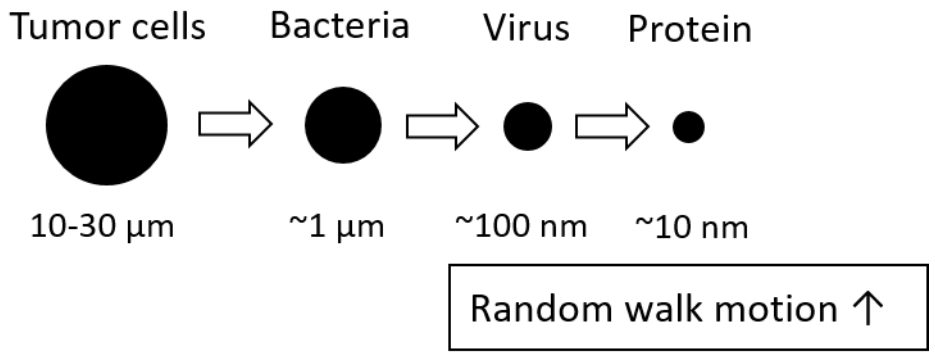


Figure 3−2. Configuration for the size of analytes.

The lateral velocity of analytes affects the binding phenomenon, mainly, and it can be induced by lift force, sedimentation, and thermal motion. As shown in Figure 3−1, as the particle size decreases, the lateral velocity induced by lift force or sedimentation decreases whereas, the thermal motion increases. Hence for a small analyte such as virus or protein, the random walk motion is dominant to describe transport of analytes inside the microfluidic channel and a transport model was presented based on Brownian motion (Figure 3−2).

From the probability density function, the probability to collide on the wall was obtained according to the height of analyte from the wall in a specific time during which the analyte travels to the observation position. By introducing an empirical coefficient for probability to collide with receptors and calculating the total number of injected analytes, the number of bound particles in the microscopic area was calculated. The empirical coefficient was obtained from the experimental results in chapter 2. The results of the calculation from the model were compared to the experimental results and verified.

## 3.2. Model description

### 3.2.1. A mathematical model for transport of analyte based on Brownian motion

The probability density function that a particle may exist at a distance (r) from the initial position after a certain time (t) is shown in Equation (3-1) by Einstein's Brownian motion as shown in Figure 3-3a [3-1]. Therefore, as shown in Figure 3-3b, the probability P(z) of a particle at a distance (z) from the channel wall to collide with the receptor by Brownian motion during a specific time (t) can be expressed as an integral form of Equation (3-1) for positions farther than z, as shown in Equation (3-2). A correction factor $C_1$ is introduced because a microscopic area is limited only to a downward direction (Figure 3-4).

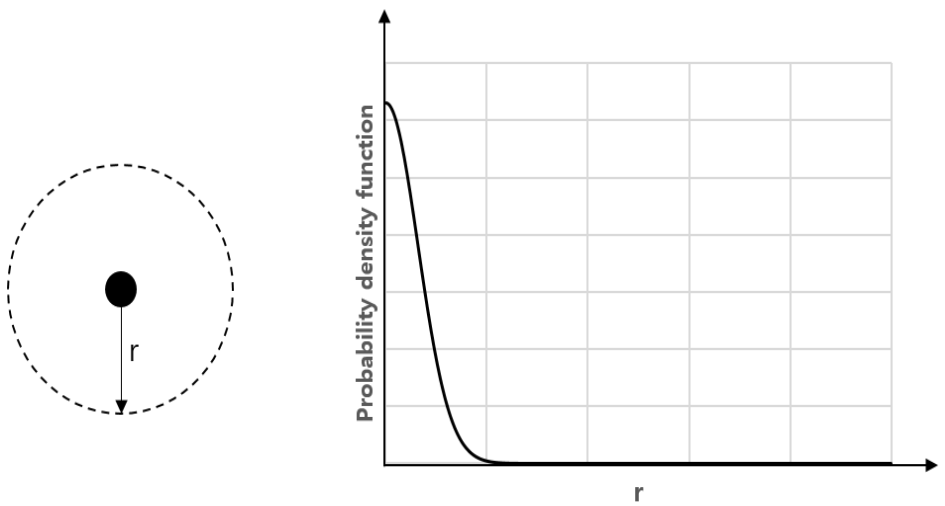


(a)

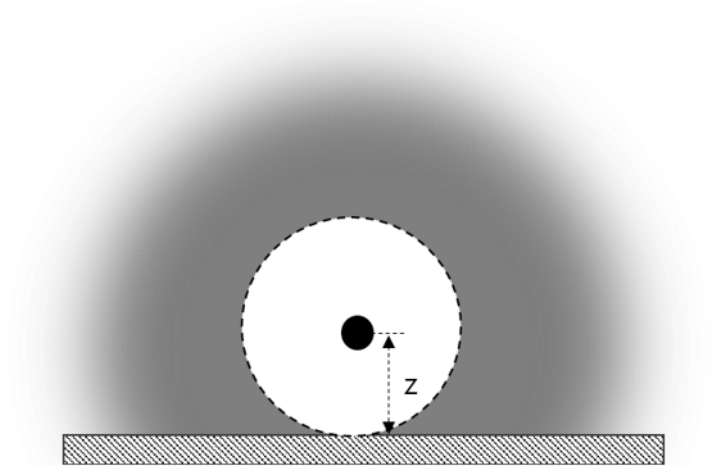


(b)

Figure 3-3. (a) The probability density function of particles existing at distance r from the initial position after t. (b) Schematic diagram of the probability that a particle at a distance of z from the channel wall will reach the wall after t.

$$p(r) = \frac{1}{\sqrt{4\pi Dt}} e^{\frac{-r^2}{4Dt}} \quad (3-1)$$

where D is the diffusion coefficient ($m^2 \cdot s^{-1}$), t is the elapsed time (s), r is the distance from the initial position of the particle (m).

$$P(z) = C_1 \int_z^{\infty} dr \frac{1}{\sqrt{4\pi Dt}} e^{\frac{-r^2}{4Dt}} \quad (3-2)$$

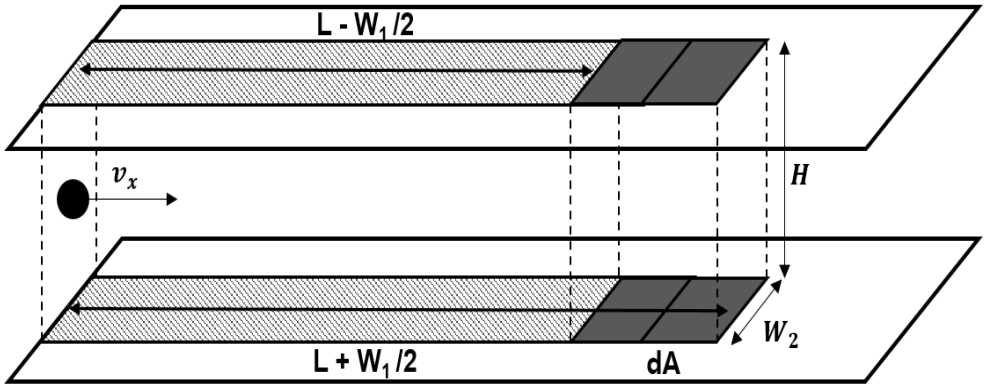


Figure 3−4. The geometrical configuration of the mathematical model for analyte−receptor binding on the microscopic area of a model description.

If the density function for the spatial distribution of analytes is expressed as f(x,y,z), the total number of particles colliding with the receptor during t is as below.

$$N_{\mathrm{H,total}} = C_1 \iiint f(x,y,z)P(z)\ dV \qquad (3-3)$$

The density function for the spatial distribution may be considered as a constant assuming that the analytes are uniformly distributed inside the microfluidic channel, and expressed as f(x,y,z) = n by using number density n.

Since not all the particles colliding with the receptor are bound, the number of particles bound to the microscopic area can be expressed as follows by introducing coefficient $C_2$ which reflects the collide−to−bound ratio and integrating it with $C_1$ into coefficient $C = C_1C_2$.

$$N_{\mathrm{bound}} = C_2 N_{\mathrm{H,total}} \qquad (3-4)$$

When the sample solution flows through the microfluidic channel, the total number of analytes involved during the detection time ( $\tau$ ) is calculated by using the number of analytes that passed through the channel cross-section. As shown in Figure 3-4, the x-directional velocity of the analyte is $v_x$, thus, the volume of the space where the total injected analytes are distributed is $W_2 \int_0^H v_x(z)\tau dz$. Therefore, the total number of injected analytes can be expressed using number density n as Equation (3-5).

$$nW_2 \int_0^H v_x(z)\tau dz \qquad (3-5)$$

In addition, t is dependent on the distance (L) from the inlet. As shown in Figure 3-4, the specific time t for the transport of analytes from the inlet to points L - $W_1/2$ and L + $W_2/2$ are $\frac{L-W_1/2}{v_x}$ and $\frac{L+W_2/2}{v_x}$, respectively. Therefore, the number of analytes bound to the microscopic area (dA) at a distance of L from the inlet can be expressed as shown below.

$$N_{\text{bound}} =$$

$$CnW_2 \left[ \int_0^H P(z)\big|_{t=\frac{L+W_1/2}{v_x}} \; v_x(z)\tau \; dz - \int_0^H P(z)\big|_{t=\frac{L-W_1/2}{v_x}} \; v_x(z)\tau \; dz \right] \qquad (3-6)$$

where n is number density ($m^{-3}$), L is the distance from inlet of microscopic area (m), H is the height of channel (m), $\tau$ is detection time (s), $v_x$ is the x-directional speed of flow ($m \cdot s^{-1}$), $W_1$ and $W_2$ are the length and width of microscopic area dA, respectively (m).

Equation (3-6) predicts the number of bound analytes using the displacement of individual particles being diffused independently by Brownian motion and the total number of injected analytes, thus, the

Brownian motion is not affected by the flow.

### 3.2.2. Diffusion coefficient of biotinylated bead

Brownian motion is affected by the temperature, the viscosity, and the radius of the analyte. The diffusion coefficient D can be calculated ($D = 2.4 \times 10^{-12}\ m^2 \cdot s^{-1}$) from the Stokes-Einstein relation as shown in Equation (3-7):

$$D = \frac{k_B T}{6\pi\eta r} \qquad (3-7)$$

where $k_B$ is the Boltzmann constant, T is the absolute temperature, $\eta$ is the viscosity, r is the radius of the analyte.

The diffusion coefficient for biotinylated beads can be also obtained, experimentally. The motion of biotinylated bead was recorded using fluorescent microscopy and the movie was sliced at an interval of 400 ms. For each image which was obtained by slicing the movie, the intensity of fluorescence was measured and the noise of signal was eliminated by setting a binary threshold. The processed intensity shows a specific pattern and it was assumed to be a circle because the biotinylated bead is spherical. Lastly, by setting and tracking the center of the imaginary circle, the movement of biotinylated bead was recorded for each frame as shown in Figure 3-5.

(a)

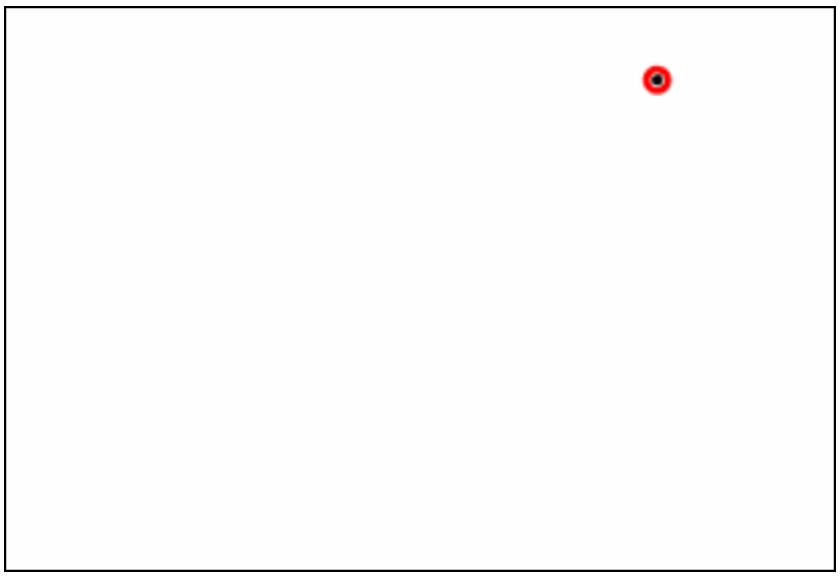

(b)

Figure 3-5. Configuration of image processing for tracking of the biotinylated bead.

The results of tracking the biotinylated bead, for example, is shown in Figure 3-6. Particle tracking was repeated in the same manner for 5 biotinylated beads and the measured diffusion coefficient was $2.2 \times 10^{-12}\ \mathrm{m^2 \cdot s^{-1}}$, which is a valid result comparing

to the calculated value from the Stokes-Einstein relation.

Moreover, hindrance effect by the wall for Brownian motion was not observed when the fluorescent microscopy was focused on 10 $\mu$m from the bottom as shown in Figure 3-4, thus, the diffusion coefficient in this study is set to be constant.

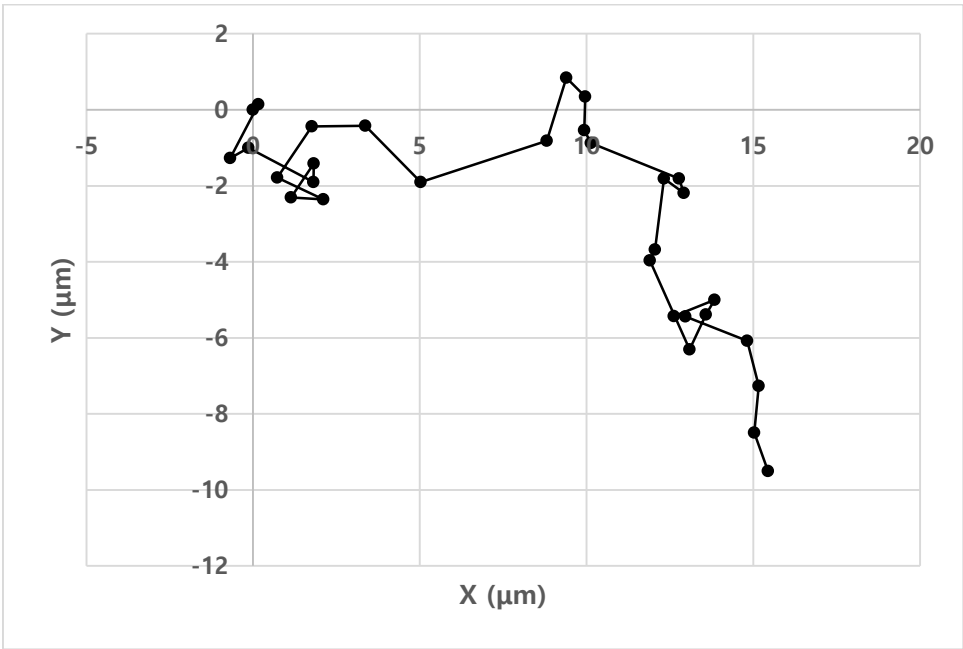


(a)

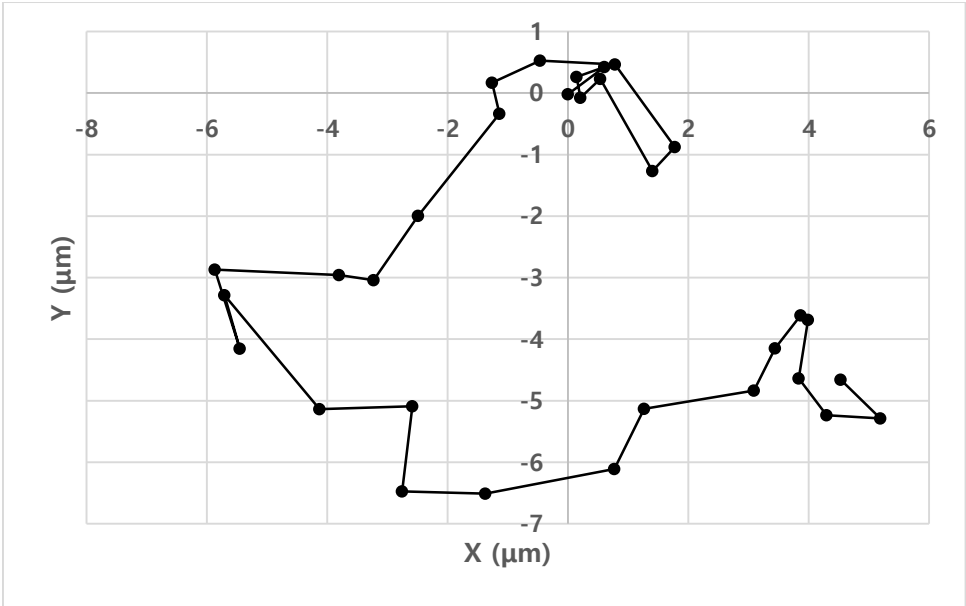


(b)

Figure 3-6. The results of tracking the biotinylated bead. The initial position was set to X=0 $\mu$m, Y=0 $\mu$m. The bead was recorded for 12 s and the focusing plane was set to (a) 50 $\mu$m from the bottom, and (b) 10 $\mu$m from the bottom

## 3.3. The empirical coefficient for mathematical model

The biotin beads mixed with the liquid sample are injected into the inlet flow along the micro-channel and pass through the microscopic area in case that they do not be bound to the receptor after colliding with the channel wall by Brownian motion during a time ($t_L$) to reach observation position (L). Therefore, $t = t_L$ in the probability density function Equation (3-1), which is the equation for calculating the number of analytes bound to the wall from the inlet to the microscopic area. Limiting the area in order to count the bound analytes to a microscopic area at a distance of L from the inlet, the number of bound analytes can be calculated as follows. The value is

calculated by the difference between the number of analytes bound to the channel surface during $t_{L+\frac{w_1}{2}}$ required to transport to the position where the microscopic area ends and the number of analytes bound to the channel surface during time $t_{L-\frac{w_1}{2}}$ required to transport to the position where the microscopic area starts. In this calculation, the specific time required for the analytes to pass through the microscopic area is $(\frac{W_1}{v_x})$, which is regardless of the position of the microscopic area (L). As the traveling time increases, the observation position (L) moves further away from the inlet so that the probability density function (Equation (3-1)) becomes broad as shown in the graph in Figure 3-7. Thus, the integral value of the probability density function, which is the probability an analyte exists over a certain distance from the initial position, increases, and the number of analytes bound to the channel surface from the inlet is thereby increased. However, although the integral value of the probability density function over a certain distance increases as t increases, the increase rate is decreased. Therefore, as t increases, the integral value for the increment $\Delta$t, that is, the number of bound analytes decreases. Therefore, as the microscopic area moves further away from the inlet, the transport time (t) of the analytes to the corresponding position increases, while the time required in order to pass through the same size of the microscopic area ($\Delta$t) is the same, resulting in a decrease in the number of analytes bound to the microscopic area.

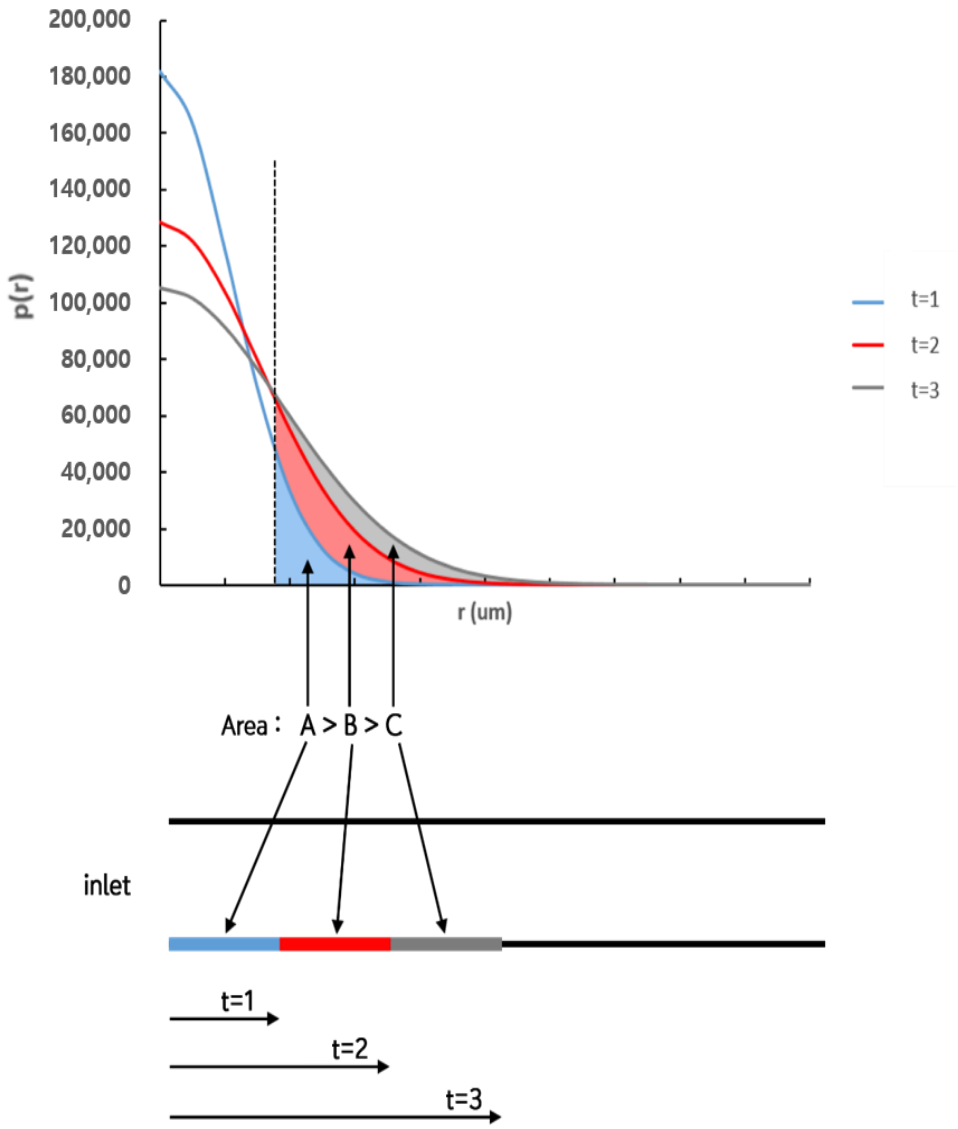


Figure 3-7. Increment of the probability of which a particle bound to the surface as time increases after being injected through the inlet to the microscopic area further off from inlet.

In order to obtain the empirical coefficient C for the mathematical model, Equation (3-6), the experimental results for the number of bound analytes normalized by number density under various

concentration conditions were used. Therefore, Equation (3−6) can be rewritten as below.

$$\frac{N_{\text{bound}}/n}{\tau} =$$

$$CW_2\left[\int_0^H P(z)\big|_{t=\frac{L+W_1/2}{v_x}}\ v_x(z)\ dz - \int_0^H P(z)\big|_{t=\frac{L-W_1/2}{v_x}}\ v_x(z)\ dz\right] \qquad (3-7)$$

In section 2.5.1, the number of normalized bound analytes increases linearly concerning $\tau$, so the slope of the linear curve corresponds to $\frac{N_{\text{bound}}/n}{\tau}$ of Equation (3−8), and the value of the empirical coefficient C can be obtained by using the slope of this curve. The slope of the master curve was $3.09 \times 10^{-15}$ which is estimated using the least square method, hence the empirical coefficient C = 0.0395. This empirical coefficient C for the mathematical model shows consistent results under other conditions.

## 3.4. Numerical estimation for the number of bound particles

### 3.4.1. Comparison of the number of bound particles from experiment and mathematical model

Comparison of the number of bound analytes from the experiment and calculated from the mathematical model is shown in Figure 3-8. For different concentration samples, the results calculated by the model show valid estimation.

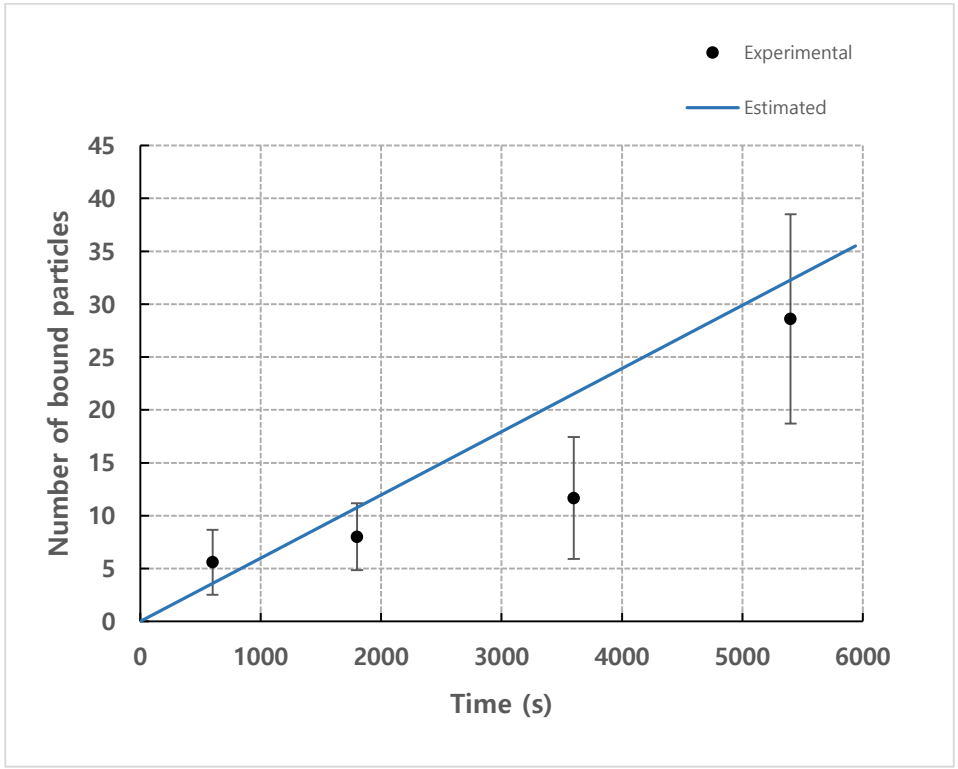


(a)

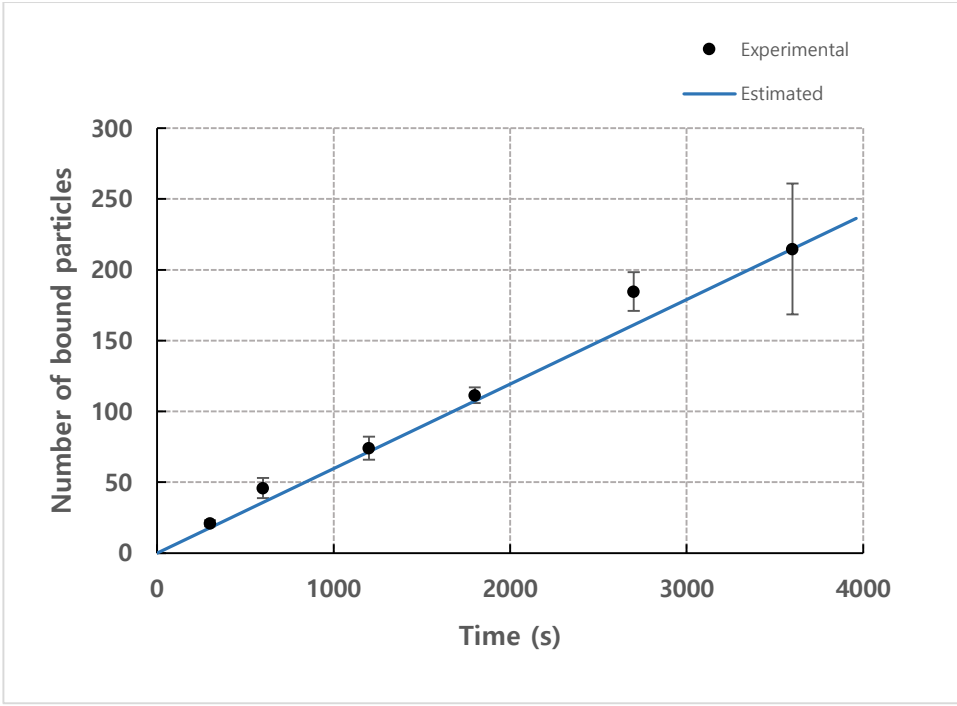
Experimental
Estimated
Number of bound particles
300
250
200
150
100
50
0
0
1000
2000
3000
4000
Time (s)

(b)

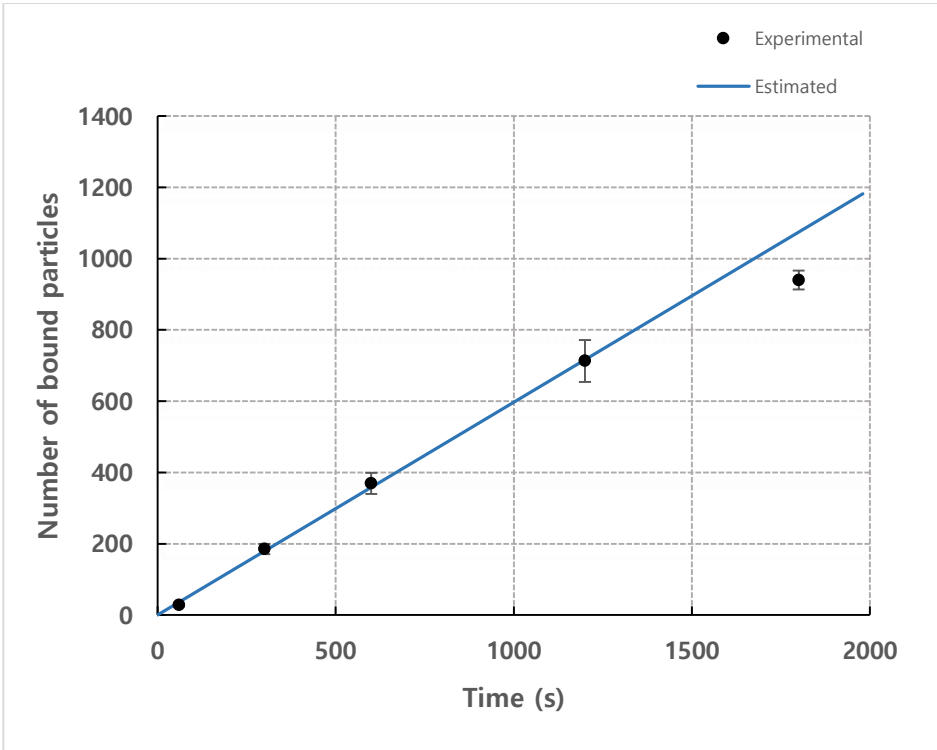
Experimental
Estimated
Number of bound particles
1400
1200
1000
800
600
400
200
0
0
500
1000
1500
2000
Time (s)

(c)

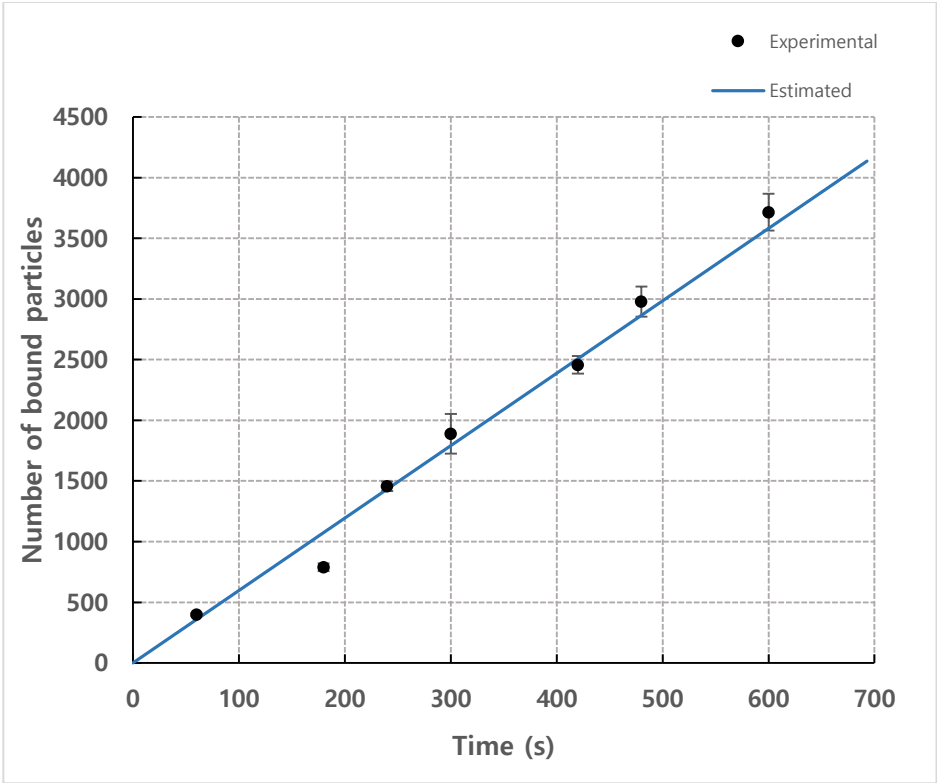


(d)

Figure 3-8. Comparison of the number of bound particles from experiment and mathematical model depending on time for different concentration of analytes (a) number density $n = 1.93 \times 10^{12}\ m^{-3}$, (b) number density $n = 1.93 \times 10^{13}\ m^{-3}$, (c) number density $n = 1.93 \times 10^{14}\ m^{-3}$, (d) number density $n = 1.93 \times 10^{14}\ m^{-3}$ (flow rate = 1.2 $mL \cdot h^{-1}$, observation position = 35 mm). Solid lines depict fitted data by the mathematical model.

The results of comparing the experimental values and calculated values by the mathematical model with different flow rates are shown in Figure 3-9. Even when the flow rate conditions were different, the mathematical model shows a valid estimation.

For a capillary flow, which is widely used in a medical diagnostic device, the flow rate is determined by the surface tension and the viscosity of the sample solution. Except for the flow front, the

velocity profile of the capillary flow coincides to that of the pressure driven flow. Thus, the mathematical model can be applied for a capillary flow in the same manner with the velocity calculated using the surface tension and viscosity of the sample.

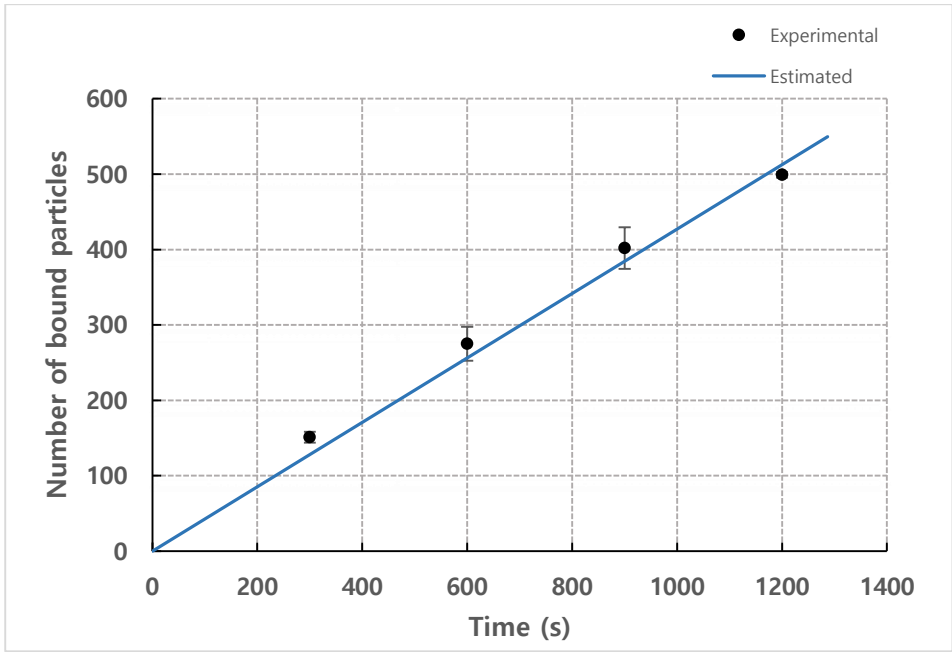


(a)

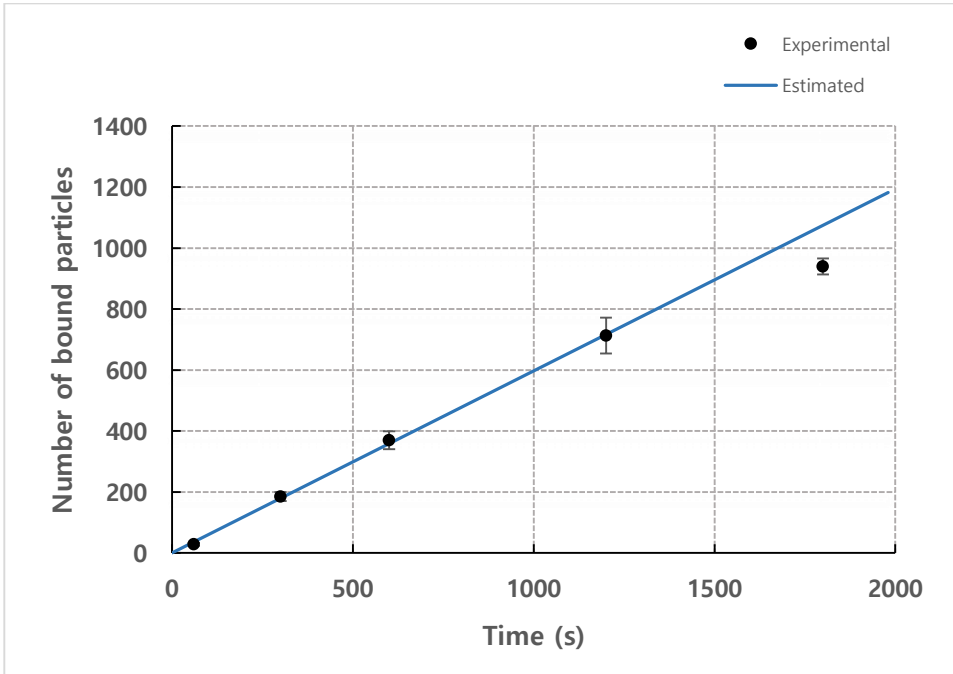


(b)

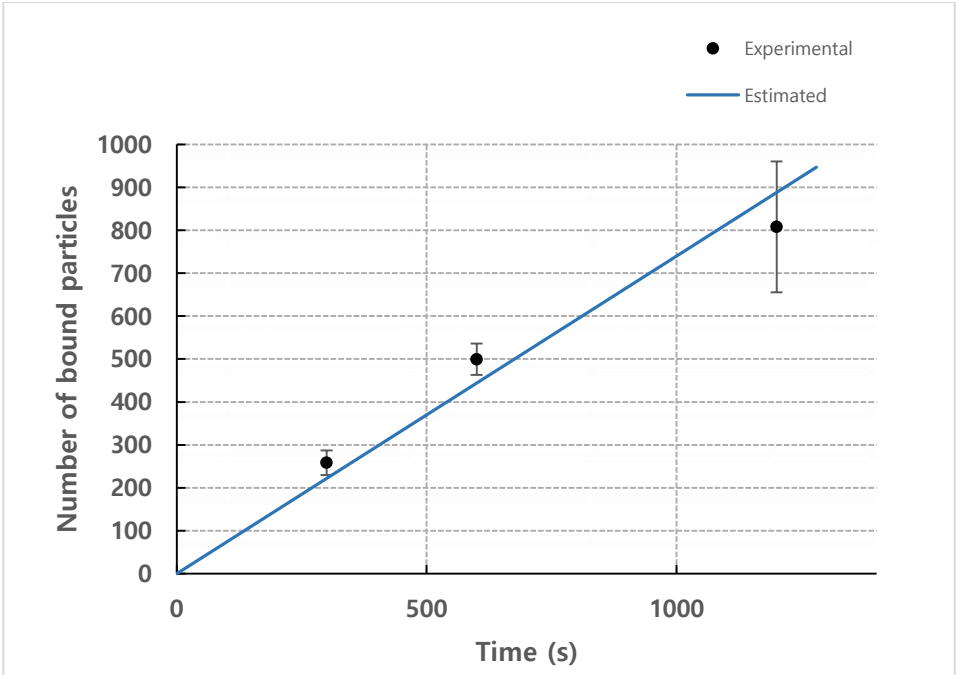


(c)

Figure 3-9. Comparison for number of bound particles from experiment and mathematical model depending on time for different flow rate condition (a) flow rate = 0.3 mL · $h^{-1}$, (b) flow rate = 1.2 mL · $h^{-1}$, (c) flow rate = 2.4 mL · $h^{-1}$ (n = $1.93 \times 10^{14}$ $m^{-3}$, observation position = 35 mm). Solid lines depict fitted data by the mathematical model. Coefficients of determination are (a) $R^2 = 0.98$, (b) $R^2 = 0.98$, (c) $R^2 = 0.93$.

### 3.4.2. Mean relative errors

In order to compare the results calculated by the mathematical model with the experimental results, the mean relative errors (MRE) for each concentration is shown in Figure 3-10 and according to it, the values calculated by the mathematical model with the empirical coefficient C obtained from the normalized data show a valid correlation with experimental values. However, in terms of number density n = $1.93 \times 10^{12}$ $m^{-3}$, the deviation between the calculated value and experimental value is relatively large. This is because the

density function for the spatial distribution of analytes cannot be assumed to be a constant for the extremely low-concentration samples. In the case of number density n = $1.93 \times 10^{12}$ $m^{-3}$, the distance between each analyte is about 80 μm and the height of the channel used in the experiment is 100 μm. Thus, as shown in Figure 3-11, only one analyte is distributed in the height direction on average in that case. Consequently, it is difficult to set the density function as constant value and a large deviation is shown.

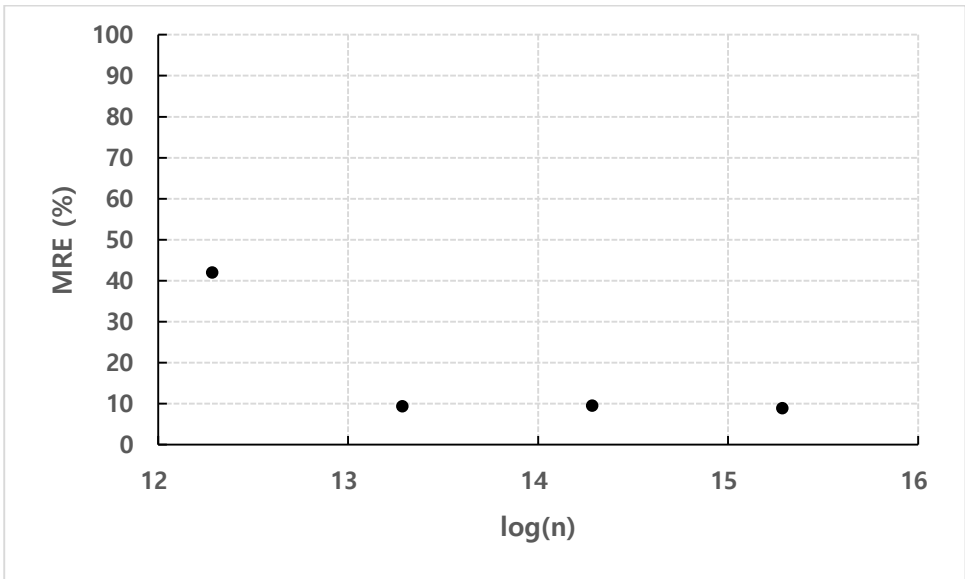


Figure 3-10. Mean relative errors (MRE) of experimental values according to the concentration and the values calculated by using the empirical coefficient C.

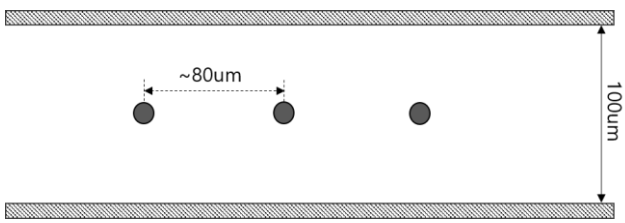


Figure 3-11. Interparticle distance when the concentration is n = $1.93 \times 10^{12}$ $m^{-3}$.

The results also show that the interaction between analyte and channel wall does not affect the distribution of particles in the channel. If repulsion between the wall and particles affects the distribution in the channel, the particles are concentrated near the center of the channel as shown in Figure 3-12b, which will reduce the binding efficiency significantly. That is, the wall-particle repulsion may act near the wall, but it is not enough to affect the distribution of particles.

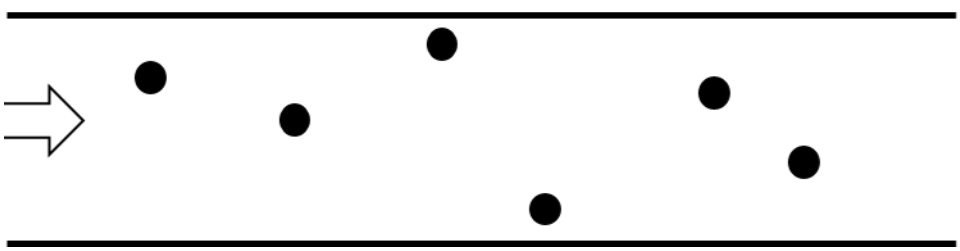

(a)

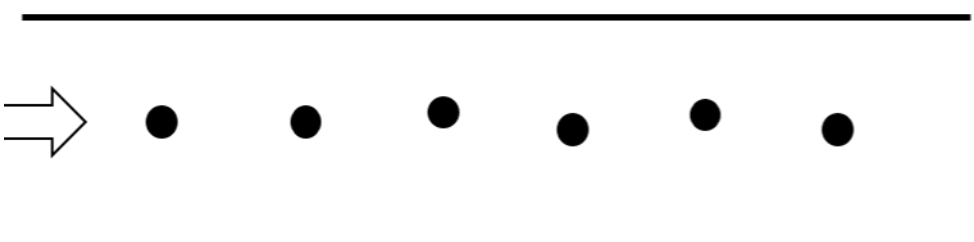

(b)

Figure 3-12. (a) Randomly dispersed particle. (b) Focused on the center of the channel due to the interaction between particle and wall.

Meanwhile, the shear-induced lift force can affect the transport of analytes towards channel wall and it is described as below [3-2].

$$F_L = K\mu V r^2 (\frac{\dot{\gamma}}{\nu})^{1/2} \quad (3-9)$$

where K is the numerical constant, $V$ is the relative velocity, r is the radius of the particle, $\dot{\gamma}$ is the shear rate, $\mu$ and $\nu$ are the dynamic and kinetic viscosity, respectively.

The maximum lift force exerted to the analyte is $6.31 \times 10^{-18}$ N from Equation (3-9) and Goldman results for the slip velocity [3-3]. For this maximum lift force, the maximum terminal velocity and time required to be accelerated at the terminal velocity are calculated as below.

$$v_{t,\max} = \frac{F_{\text{lift}}}{6\pi\mu r} \sim 3.35 \text{ nm/s} \quad (3-10)$$

$$\text{T} = \frac{m}{6\pi\mu r} \sim 2 \times 10^{-12} \text{ s} \quad (3-11)$$

Considering that it is the maximum value and it is dissipated as the analyte moves away from the channel wall, the effect by the shear force can be neglected.

### 3.4.3. Effect of observation position from inlet and channel height

Figure 3-13 shows the results of comparing the calculated values from the mathematical model with the experimental results depending on the observation position for number density n = $1.93 \times 10^{14}$ $\text{m}^{-3}$ and flow rate = 1.2 mL/h. As shown in Figure 3-13a, the mathematical model shows a valid estimation for the different observation positions. Figure 3-13b shows the result of plotting the number of bound analytes according to the observation position when

fixing the detection time to 20 min. As in the experimental results, the number of bound analytes exponentially decreases as the observation position moves further away from the inlet.

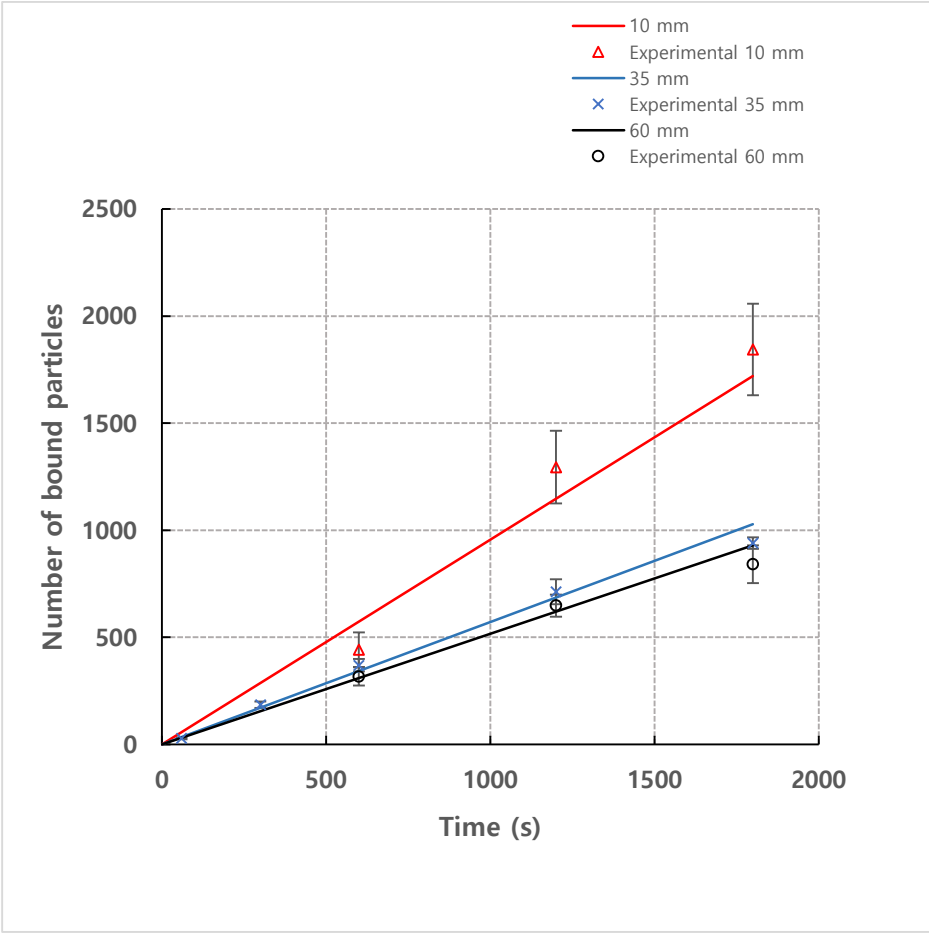


(a)

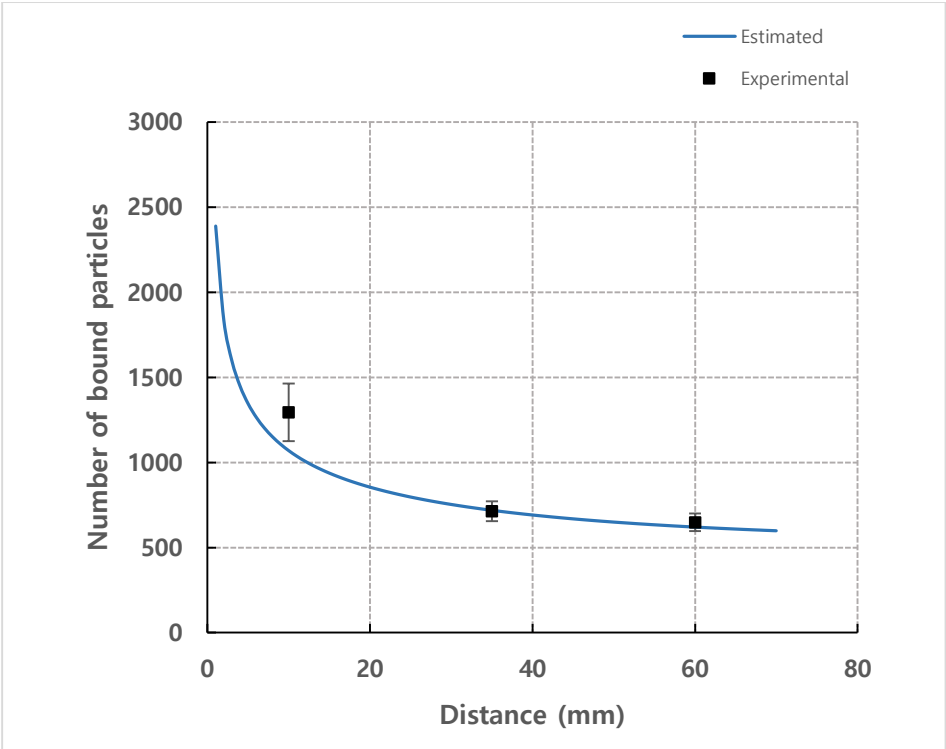


(b)

Figure 3-13. Comparison for number of bound particles from experiment and mathematical model for n = $1.93 \times 10^{14}$ $m^{-3}$, flow rate = 1.2 mL · $h^{-1}$. (a) depending on observation position (Coefficients of determination are $R^2 = 0.95$ for 10 mm, $R^2 = 0.98$ for 35 mm and $R^2 = 0.94$ for 60 mm), (b) when detection time is set to 20 min. (C = 0.0395, D = $2.4 \times 10^{-12}$ $m^2 \cdot s^{-1}$, $W_1$ = 1362 μm, $W_2$ = 1021 μm).

On the other hand, as shown in Figure 3-14, the binding efficiency according to the channel height is obtained by extrapolating the mathematical model under the following conditions, the detection time is 20 min and the average x-direction velocity ($\overline{v_x}$) is 0.67 mm · $s^{-1}$, which corresponds to the value at flow rate 1.2 mL · $h^{-1}$ for 100 μm height channel. In this calculation, the binding efficiency is calculated by normalizing the number of bound analytes by the total number of injected analytes. As shown in Figure 3-14a,

in the case that the observation position is the inlet, the binding efficiency increases as the channel height decreases. This is because the distance required to be transported to channel wall decreases as the height of channel decreases while the mobility by Brownian motion remains the same, regardless of the channel height. On the other hand, when the observation position is 35 mm away from the inlet, the peak for binding efficiency is shifted as shown in Figure 3-14b. As the channel height decreases, the probability to be bound around the inlet increases so that fewer analytes traveled around the downstream of the channel. For the higher channels, only particles closer to the wall can be bound to the channel surface around the inlet and more particles pass through the inlet area. The optimal channel height to maximize the binding efficiency tends to increase as the observation position moves further away from the inlet. Therefore, if the scanning area is set to a certain distance from the inlet, the channel should be designed by considering the optimal value of the binding probability according to the observation position.

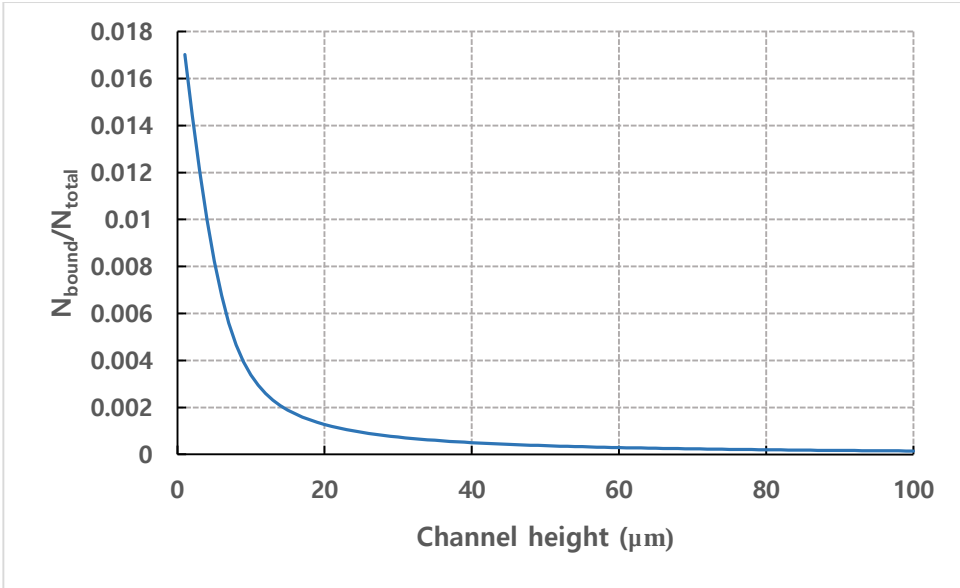


(a)

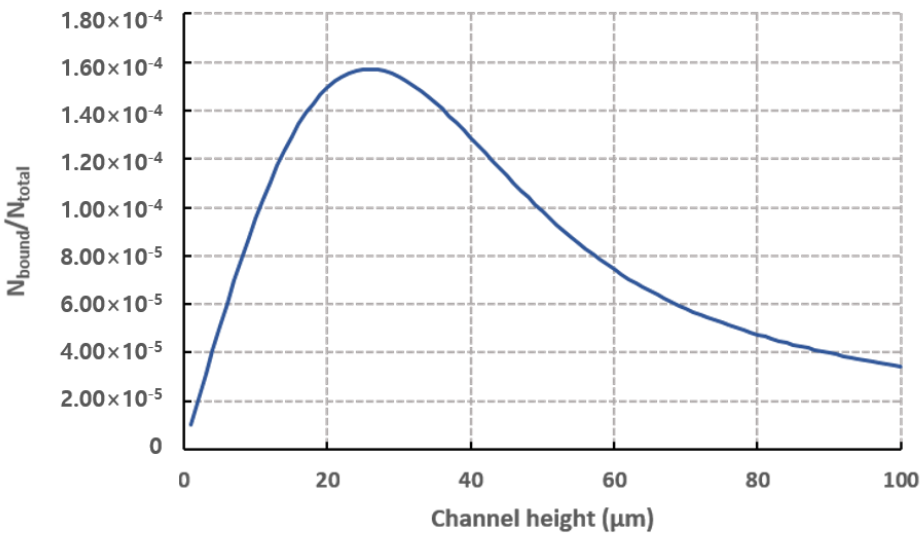


(b)

Figure 3-14. $N_{bound}/N_{total}$ according to the channel height for (a) observation position = 0 mm (b) observation position = 35 mm.

## Reference

[3-1] Kätelhön, E.; Sokolov, S.V.; Compton, R.G. Near-wall hindered diffusion: Implications for surface-based sensors. *Sens. Actuators B Chem.* 2016, *234*, 420-425.

[3-2] Zheng, X.; Silber-Li, Z. The influence of Saffman lift force on nanoparticle concentration distribution near a wall. *Appl. Phys. Lett.* 2009, *95*, 124105.

[3-3] Goldman, A.; Cox, R.; Brenner, H. Slow viscous motion of a sphere parallel to a plane wall—II Couette flow. *Chem. Eng. Sci.* 1967, *22*, 653-660.

# Chapter 4. Enhancement of sensitivity using dummy particles

## 4.1. Overview

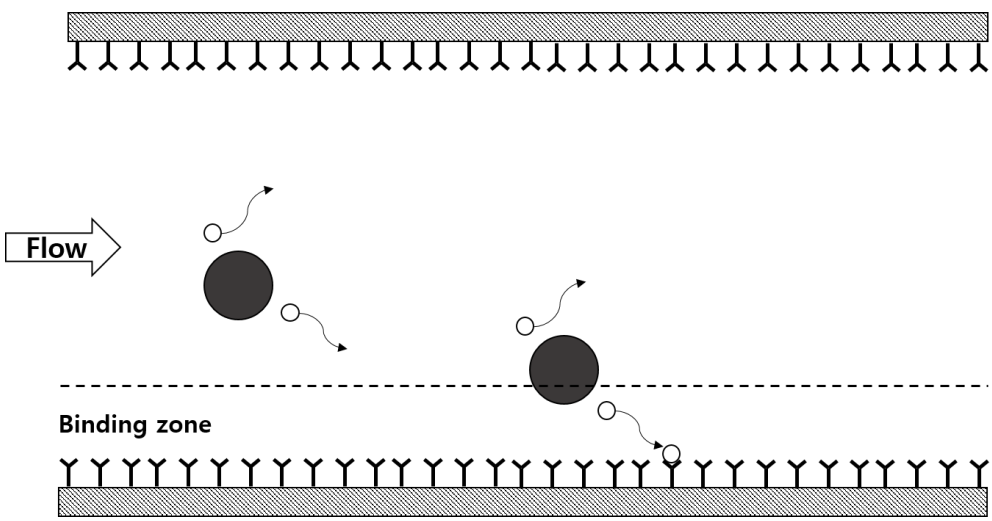


Figure 4-1. The schematic diagram for enhancement of analyte transport towards the wall using dummy particles.

In order to enhance analyte transport towards the wall, dummy particles were added to the sample solution. When dummy particles are pumped to the microchannel, it rotates by the shear flow and its rotation generates lateral flow locally [4-1,4-2]. Moreover, a suspension of particles induces normal stresses and pushes analytes in the lateral direction as they pass by, which is a fluid effect, not a collision [4-3,4-4,4-5]. Although the lateral flow by dummy particles is not unidirectional towards the wall, it can enhance the binding of analytes with receptors since the binding process is almost irreversible. Inside the binding zone, in which analytes are favorable

to be bound to the receptors, the effect of dummy particles is not symmetry as shown in Figure 4-1. Besides, because the rotational speed of dummy particles increases as the particles approaches to the wall, binding enhancement using dummy particles is effective.

In this chapter, the experimental setup and results were presented first. The experiments were performed in two parts: Observation of rotational motion of dummy particle, Binding enhancement using dummy particles. The methods for each experiment were shown in Figure 4-2. In observation of rotational motion tests, ellipsoidal particles were prepared as a dummy particle by stretching spherical PS particles and the tests were performed in Polydimethylsiloxane (PDMS) channel through the high-speed camera. In the binding enhancement using dummy particle test, Poly(methyl methacrylate) (PMMA) microchannel was used which is the same channel used in Chapter 2. As the dummy particles, 3 $\mu$m and 10 $\mu$m PS particle were used which do not have the fluorescent label in order not to be detected through fluorescence microscopy, whereas, the biotinylated bead were labeled by fluorescence which was used as an analyte.

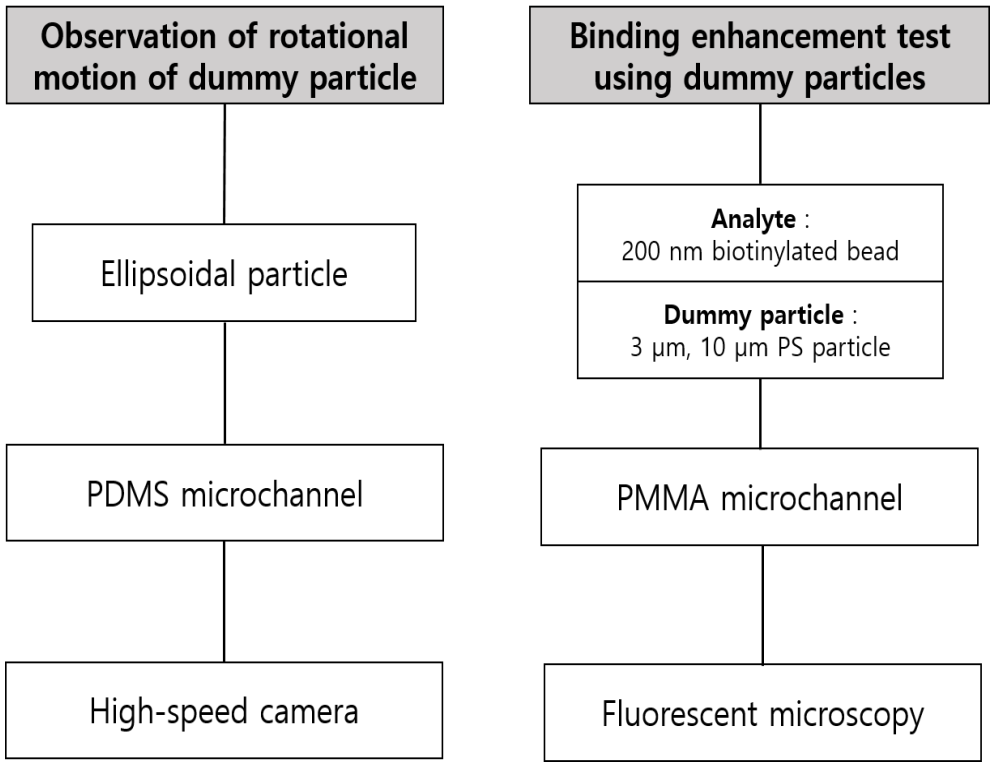


Figure 4-2. Illustration of experiments.

## 4.2. Rotational motion of dummy particles

### 4.2.1. Fabrication of microfluidic channel

The microfluidic channels were fabricated using soft lithography which was frequently used in microchannel fabrication due to its convenient and cost-effective properties. Master mold for soft lithography was made through photolithography using SU-8 negative photoresist. Mixed Sylgard 184 pre-polymer and curing agent were degassed and poured into a master mold with mass ratio 1/10. After the curing process at 60 ℃ in a convection oven for 12 hours, the PDMS replica was peeled off and it was bonded to a glass slide using oxygen plasma treatment. The oxygen plasma was treated with 60 W

for 40 s and the baking process was followed for 2 hours at 60 ℃ in the convection oven. The height and width of the PDMS microchannel were set to 500 ㎛ and 100 ㎛, respectively, as shown in Figure 4-3.

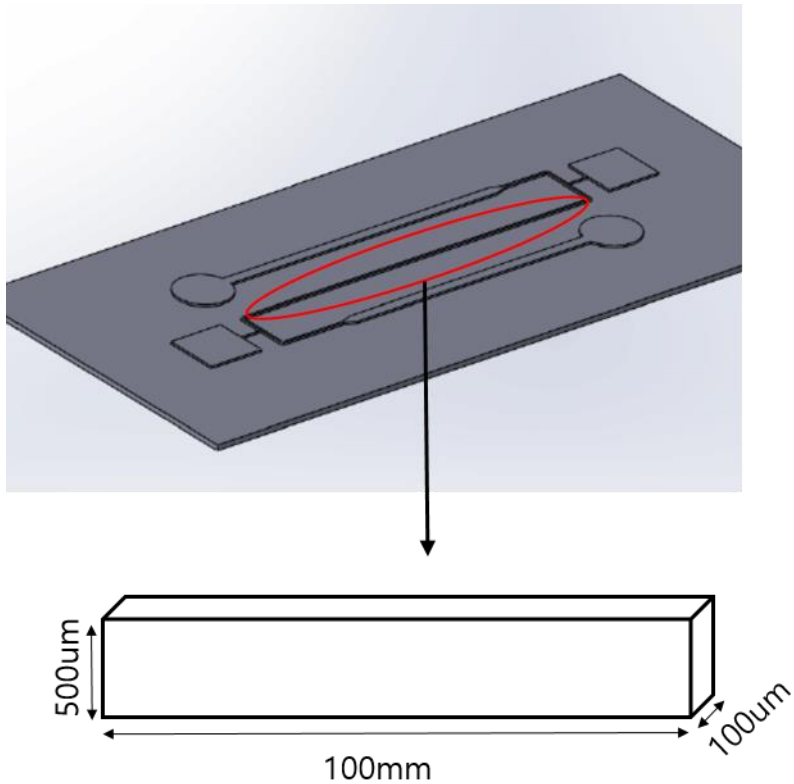


Figure 4-3. The dimension of PDMS microfluidic channel.

### 4.2.2. Dummy particle preparation

Ellipsoidal particles were produced by stretching spherical PS particles which of diameter was 10 ㎛. Firstly, PVA film was manufactured in which PS particles were embedded. Particle embedded PVA film was stretched up to 120% strain in the oil bath at 145° C. The recovered film was washed with IPA and soaked in DI water overnight in order that residual PVA was completely dissolved. The deformed PS particles were obtained by high-speed

centrifugation. The image of the prepared ellipsoidal particle is shown in Figure 4-4.

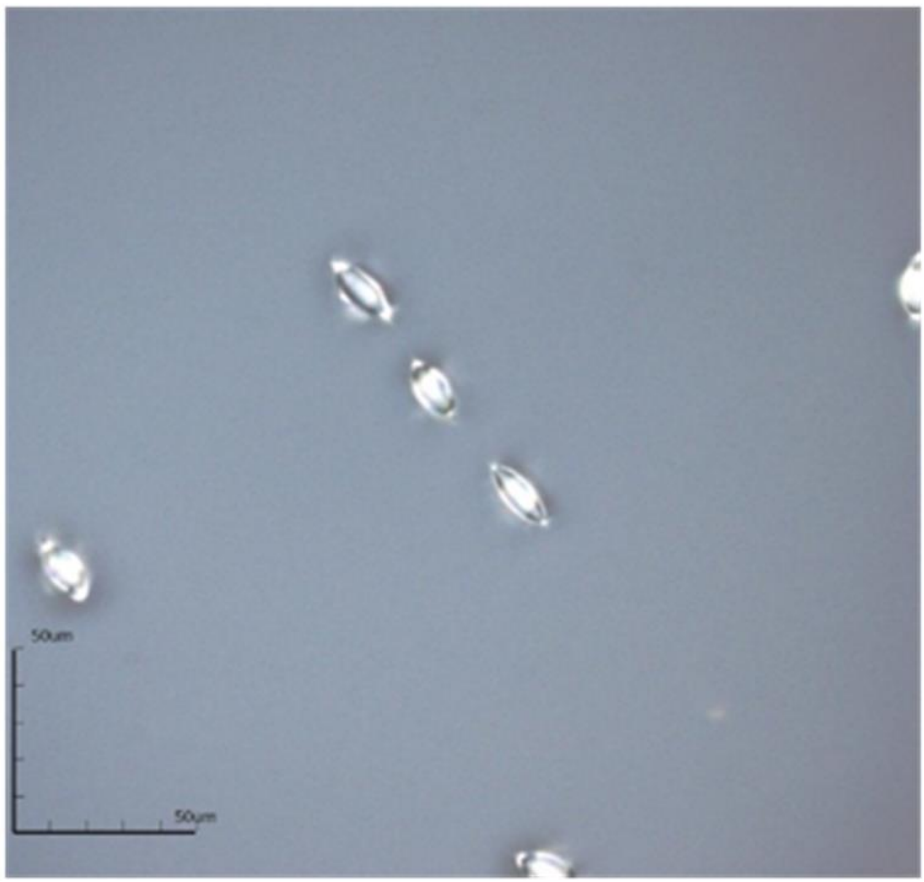


Figure 4-4. Microscopic image of ellipsoidal particles. The ellipsoidal particles were manufactured by stretching and recovering 10 μm PS particles.

### 4.2.3. Observation of rotational motion of dummy particles in PDMS channel

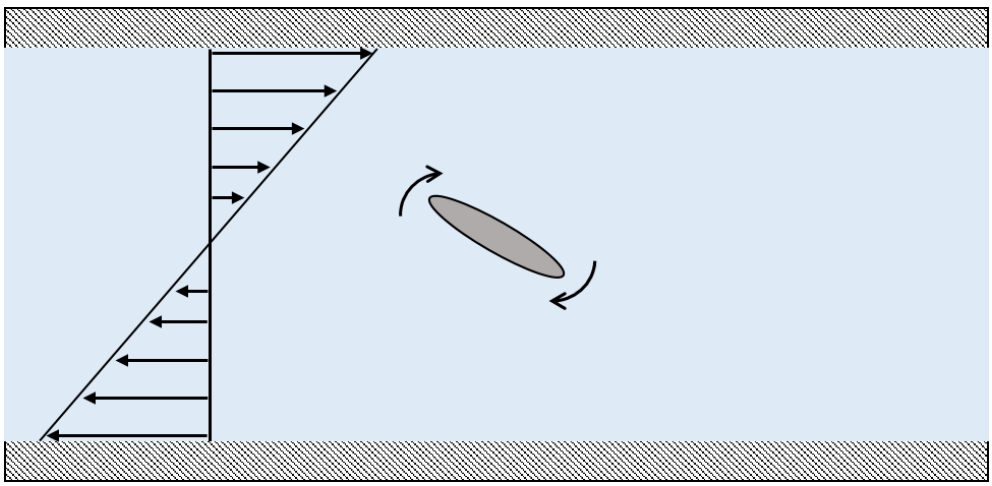

Figure 4-5. Illustration of rotational motion of a particle suspended in fluid for simple shear flow.

Jeffery suggested the model of rotational motion of the particle in simple shear flow as shown in Figure 4-5 and exact solutions for the angle and angular speed are [4-6]

$$\varnothing = tan^{-1}\left(\frac{b}{a}tan\frac{abGt}{a^2+b^2}\right) \quad (4-1)$$

$$\dot{\varnothing} = \frac{G}{a^2+b^2}\left(b^2cos^2\varnothing + a^2sin^2\varnothing\right) \quad (4-2)$$

where $\varnothing$ is the orientation angle, G is the shear rate, a and b are the minor semi axis and the major axis of the particle, respectively.

Jeffery model describes the rotational motion of particles for simple shear flow. So the shear rate in this case, which is not a simple shear flow but the Poiseuille flow, is assumed to be that of value at the center of the particle as shown in Figure 4-6.

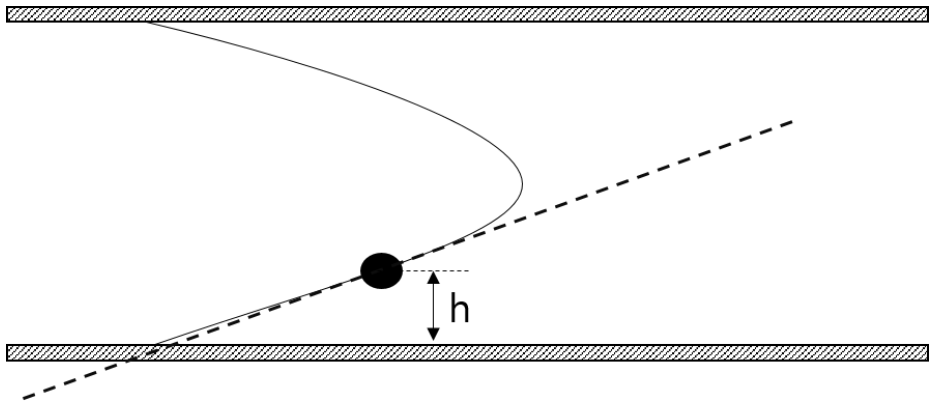


Figure 4-6. Shear rate assumption for application of Jeffery model.

The rotational speed of spherical particles is difficult to measure since the rotational motion of the particle is not distinct even through the high-speed camera. The rotation angle was clearly detected in the case of ellipsoidal particles, so the rotational motion was observed using ellipsoidal PS particles. In order to observe the rotational motion of dummy particle, a high speed camera (IDT MotionXtra N3) was mounted to microscopy and the motion was recorded under 400 Hz condition. The results are compared with the Jeffery model as shown in Figure 4-7.

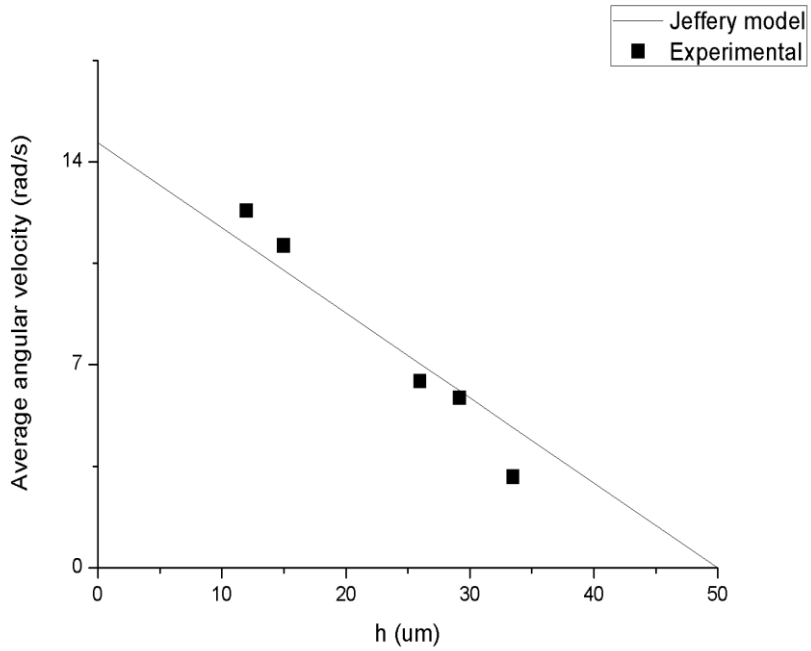


Figure 4-7. Comparison of measured angular velocity with the Jeffery model. Rotational motion of the dummy particle was observed by the high-speed camera using PDMS microfluidic channel. Angular velocity for Jeffery model was calculated using Equation (4-2).

## 4.3. The number of bound particles with dummy particles

### 4.3.1. Experimental methods

The binding enhancement test was performed in PMMA microchannel which is the same channel in Chapter 2. To examine the effect of dummy particles for the analyte-receptor binding efficiency, streptavidin was immobilized at the channel wall as the receptors in the same manner. 200 nm polystyrene beads (FluoSpheres™ Biotin-Labeled Microspheres) were used as the analytes which were biotinylated for binding with Streptavidin and labeled with fluorescent dye so that it can be detectable under the

fluorescence microscope. 3 μm and 10 μm polystyrene particles were used as dummy particles to enhance the lateral movement of biotinylated beads. Their surfaces had no functional group that interacts with streptavidin or fluorescent dye to prevent noise from the dummy particles.

The experimental conditions are shown in Table 4-1. Biotinylated beads tagged with fluorescent dye were mixed with deionized water for sample fluid. Besides, 0.001 to 0.037 volume fraction of dummy particles were added to the sample fluid. The concentration of biotinylated beads was 85.7 $ng \cdot ml^{-1}$ which is equivalent to the number density $1.93 \times 10^{13}\ m^{-3}$. Considering that the inter-particle distance is about 37 μm and the height of the channel is 100 μm, two or three biotinylated beads are distributed in the height direction on average.

The sample solution flowed through the micro-channel for 10 minutes followed by 1 minute of washing the micro-channel to remove unbound analytes from the channel. A syringe pump was used to control flow rate ($0.6ml \cdot h^{-1}$, $1.2ml \cdot h^{-1}$, $2.4ml \cdot h^{-1}$). In the case of 1.2 $ml \cdot h^{-1}$, the average velocity of the flow ($\overline{u}$) is equivalent to about 0.67 $mm \cdot s^{-1}$. After this biotinylated beads-streptavidin binding process, a fluorescent microscope is used to count the number of biotinylated beads tagged with fluorescent dye bound on the micro-channel wall where the streptavidin fixed previously. The length and width of the microscopic area were 1362 μm and 1021 μm, respectively, which were same in chapter 2. Image processing was also performed in the same manner. After setting a binary threshold to remove the noise and image processing for the uniform signals of the fluorescence image for the particle, the number for particles

bound in the microscopic area were counted discretely. This whole test was repeated 5 times for the same conditions.

Table 4-1. Experimental conditions

| Flow rate | Dummy particle volume fraction | Dummy particle diameter |
|---|---|---|
| 0.6 ml/h | 0 | |
| 1.2 ml/h | 0 | |
| 2.4 ml/h | 0 | |
| 1.2 ml/h | 0.003 | 3 μm |
| 1.2 ml/h | 0.005 | 3 μm |
| 1.2 ml/h | 0.01 | 3 μm |
| 1.2 ml/h | 0.03 | 3 μm |
| 0.6 ml/h | 0.001 | 3 μm |
| 2.4 ml/h | 0.001 | 3 μm |
| 1.2 ml/h | 0.11 | 10 μm |

### 4.3.2. Effect of dummy particle volume fraction

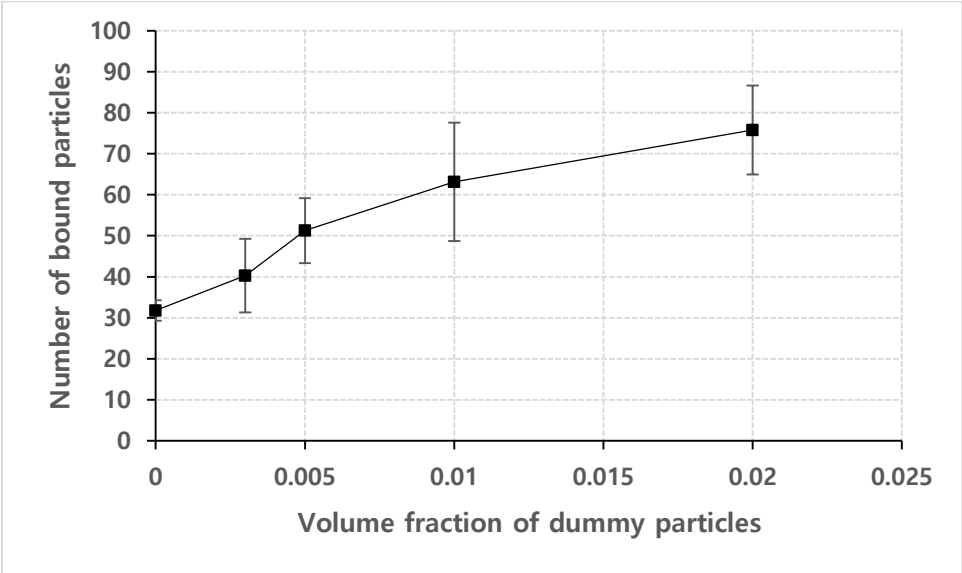


Figure 4−8. The number of bound particles depending on the volume fraction of 3μm dummy particles (number density of analytes n=$1.93 \times 10^{13}\ m^{-3}$, Flow rate=1.2 $mlh^{-1}$, detection time $\tau$ =600 s).

The number of bound particles increased with the addition of dummy particles as shown in Figure 4−8. The linearity is maintained for a small volume fraction of dummy particles but as the volume fraction of dummy particles increases, it is saturated. This can be confirmed clearly in Figure 4−9, which shows the increased number of bound particles depending on the volume fraction of dummy particles.

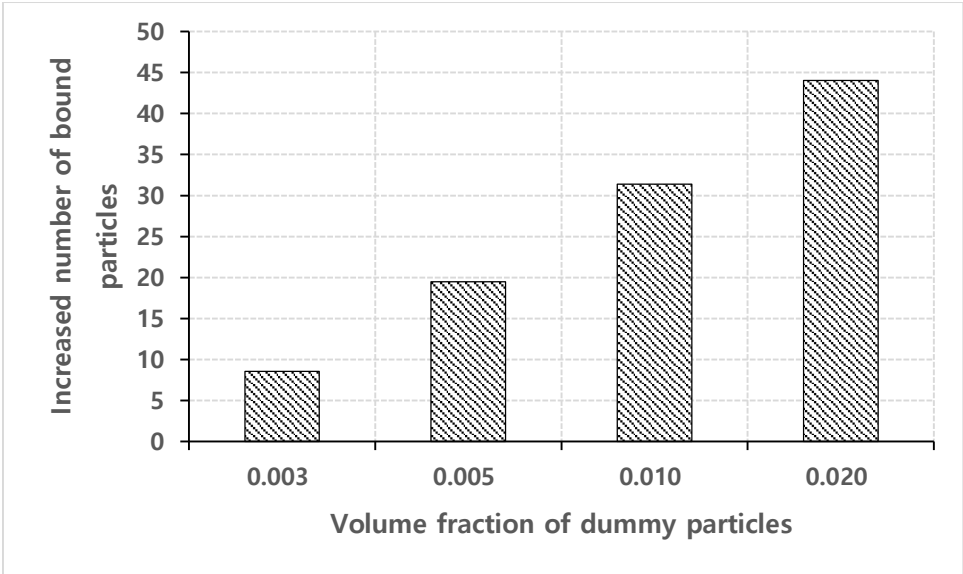


Figure 4−9. Increased number of bound particles depending on the volume fraction of 3 μm dummy particles (n=$1.93 \times 10^{13}\ m^{-3}$, Flow rate=1.2 $mlh^{-1}$, $\tau$ =600 s).

For 0.01 volume fraction of 3 μm dummy particles, number density $n_d$ is $7 \times 10^{14}\ m^{-3}$. Assuming that the dummy particles are distributed uniformly so that the volume occupied by each dummy particles is identical, the inter−particle distance is about 11 μm (Figure 4−10). Within that distance, dummy particles affect each other and the effect of dummy particles is saturated for large volume fraction. Moreover, its rotational motion is retarded by adjacent particles.

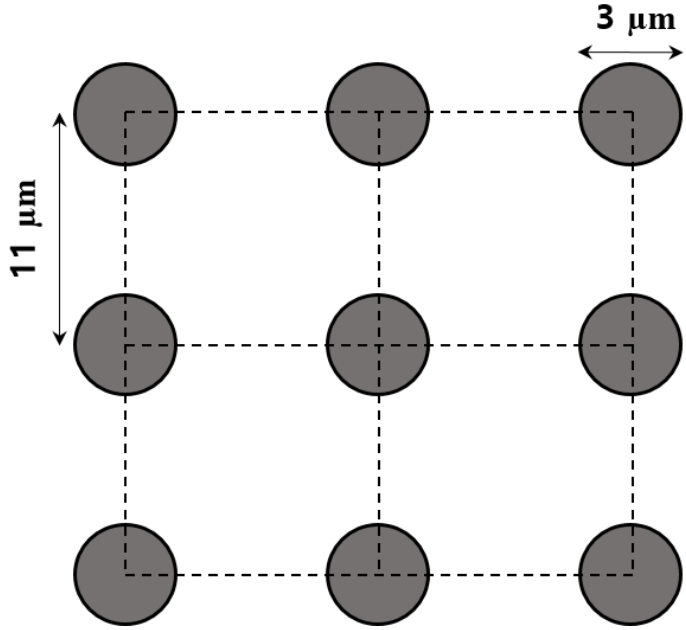


Figure 4−10. Inter−particle distance for $n_d$=$7 \times 10^{14}\ m^{-3}$.

### 4.3.3. Effect of flow rate and dummy particle size

Figure 4−11a shows the result of plotting the number of bound particles for each flow rate under the conditions of n=$1.93 \times 10^{13}\ m^{-3}$ and $\tau$ =600 s without dummy particles. The number of bound particles increased slightly over flow rate but the increase rate is not linear to the total injected number of analytes. With 0.003 volume fraction of 3 μm dummy particles, the number of bound particles is shown in Figure 4−11b. Comparing to the case without dummy particles, the more analytes were bound to the wall over flow rate.

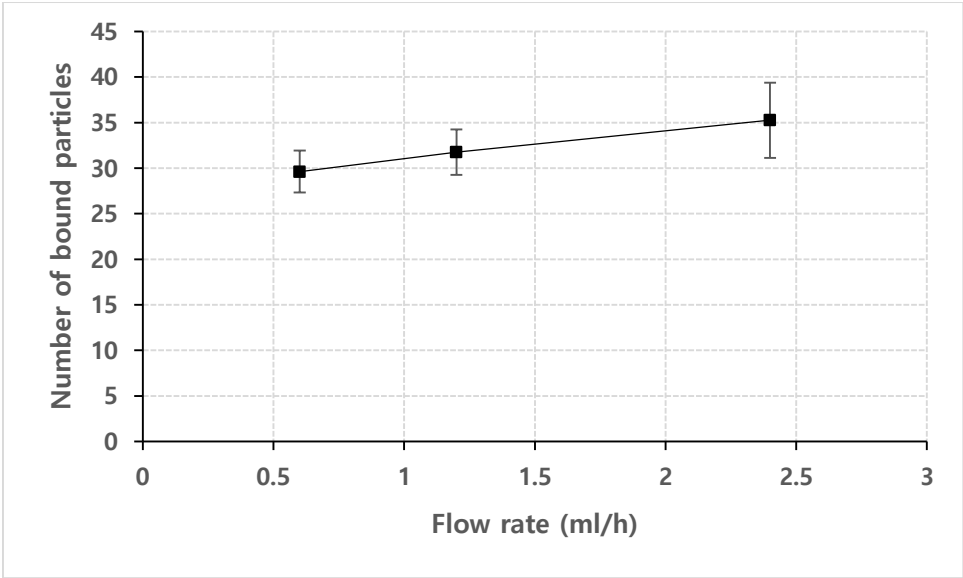


(a)

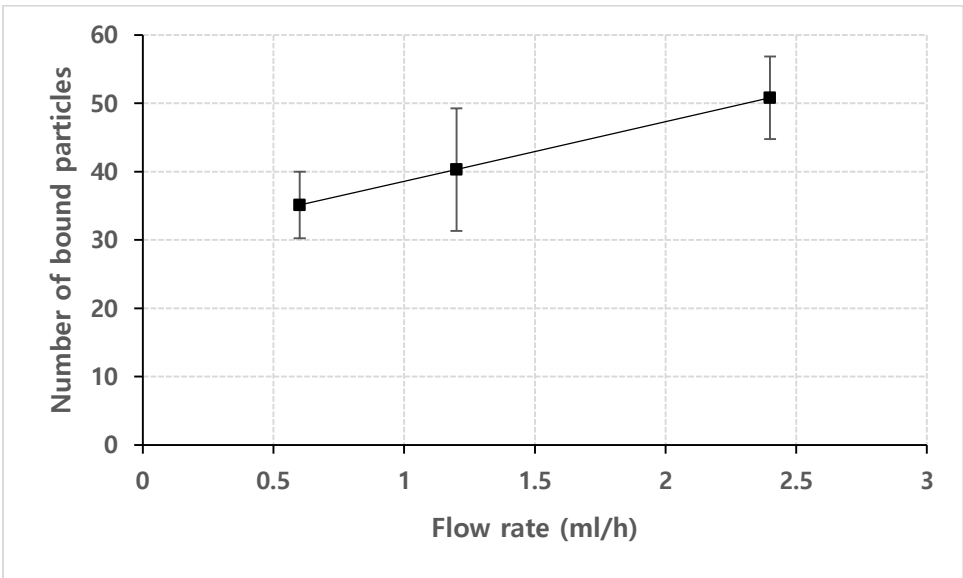


(b)

Figure 4-11. (a) The number of bound particles depending on flow rate without dummy particles (n=$1.93 \times 10^{13}\ m^{-3}$, $\tau$ =600 s), (b) Number of bound particles depending on flow rate with 3μm dummy particles (n=$1.93 \times 10^{13}\ m^{-3}$, The volume fraction of 3 μm dummy particles=0.003, $\tau$ =600 s).

The increased number of bound particles according to flow rate is shown in Figure 4−12a and the effect of dummy particles increased as the flow rate increased. The increased number is calculated from each case of flow rate without dummy particles, separately. The shear rate in the channel over the distance from the bottom wall for each flow rate is shown in Figure 4−12b. As the shear rate increases, the dummy particles rotate faster, so that more lateral flow is generated.

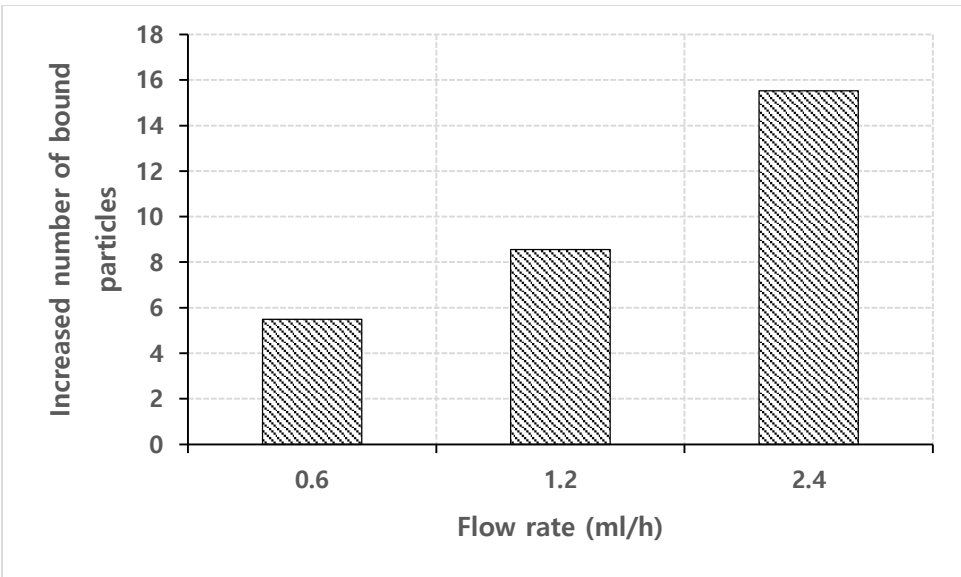


(a)

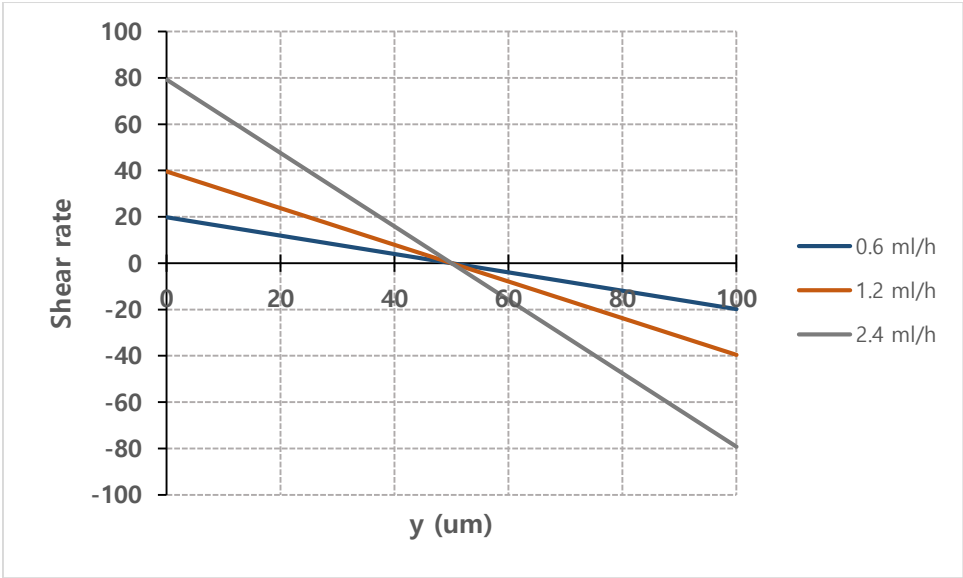


(b)

Figure 4-12. (a) The increased number of bound particles depending on flow rate with 3μm dummy particles (n=$1.93 \times 10^{13}\ m^{-3}$, The volume fraction of 3 μm dummy particles=0.003, $\tau$ =600 s), (b) Shear rate according to the distance from the bottom wall for each flow rate.

The increased number of bound particles depending on the dummy particle diameter is shown in Figure 4-13. For 10 μm dummy particles, 0.11 volume fraction was added so that the number density is coincident with that of 3 μm dummy particles. With the same number density of dummy particles, the more analytes were bound to the wall in case that 10 μm dummy particles were added and the increment is linear to the diameter of dummy particles.

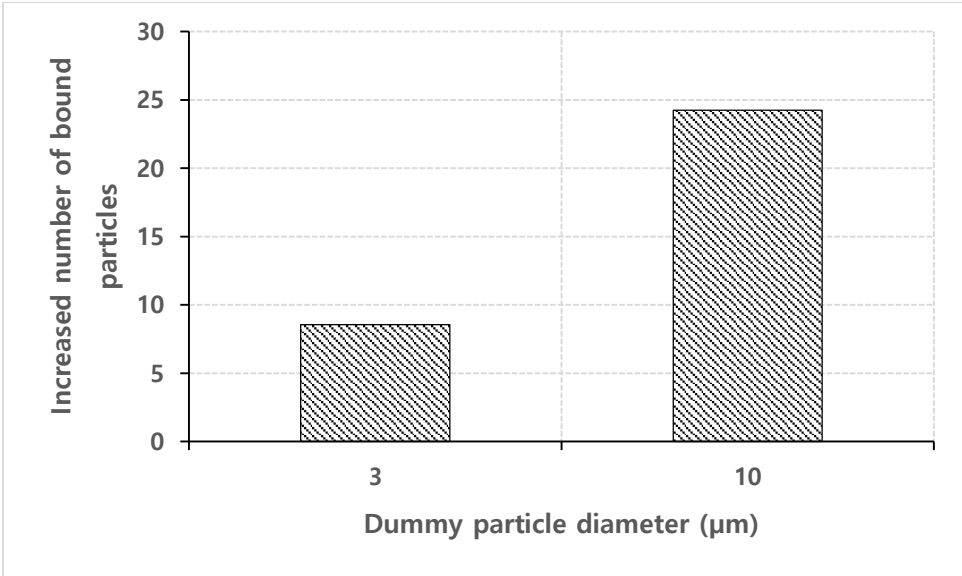


Figure 4−13. The increased number of bound particles according to the diameter of dummy particles. (n= $1.93 \times 10^{13}\ m^{-3}$, $n_d$= $2.1 \times 10^{14}\ m^{-3}$, flow rate=1.2 $mlh^{-1}$, $\tau$ =600 s).

## Reference

[4-1] Jeffery, G. B., The motion of ellipsoidal particles immersed in a viscous fluid. Proceedings of the Royal Society of London. Series A, Containing papers of a mathematical and physical character 1922, 102 (715), 161-179.

[4-2] Bretherton, F. P., The motion of rigid particles in a shear flow at low Reynolds number. *Journal of Fluid Mechanics* 1962, *14* (2), 284-304.

[4-3] Semwogerere, D.; Weeks, E. R., Shear-induced particle migration in binary colloidal suspensions. *Physics of Fluids* 2008, *20* (4), 043306.

[4-4] Frank, M.; Anderson, D.; Weeks, E. R.; Morris, J. F., Particle migration in pressure-driven flow of a Brownian suspension. *Journal of Fluid Mechanics* 2003, *493*, 363-378.

[4-5] Semwogerere, D.; Morris, J. F.; Weeks, E. R., Development of particle migration in pressure-driven flow of a Brownian suspension. *Journal of Fluid Mechanics* 2007, *581*, 437-451.

# Chapter 5. Analysis of the dummy particle effect

## 5.1. Overview

In Chapter 4, an experimental study was presented about the enhancement of analyte transport towards the wall using dummy particles. In this chapter, analysis of the enhancement of analyte transport was demonstrated. The lateral flow induced by dummy particle was examined, numerically, and the increased number of particles was estimated by setting binding zone from DLVO theory named after Boris Derjaguin and Lev Landau, Evert Verwey and Theodoor Overbeek.

## 5.2. Model description

### 5.2.1. Depth of binding zone

The DLVO (Derjaguin, Landau, Verwey, Overbeek) theory described the interaction between colloidal particles dispersed in an electrolyte by calculating a short-ranged van der Waals interaction and an electrostatic repulsion [5-1,5-2]. But it also can be used to describe the interaction between the wall surface and an analyte in order to set a binding zone in which analyte is assumed to be bound to the wall.

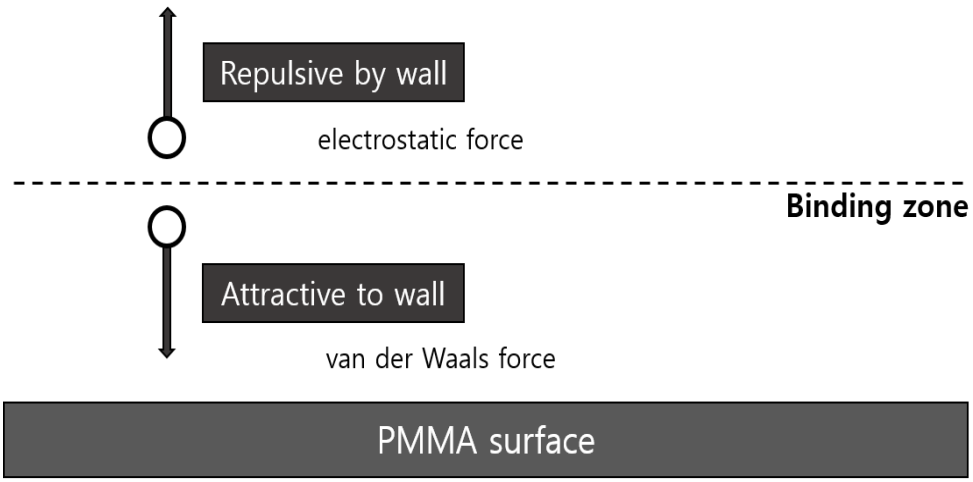


Figure 5-1. Illustration of the boundary for the binding zone in which the analyte is bound to the receptor, immediately. The analyte is repulsed by the wall through electrostatic force and attracted to the wall through van der Waals force.

There are repulsive force and attractive force for the interaction between the wall surface and a single analyte as shown in Figure 5-1. The attractive force is van der Waals force $F_{VW}$ and it is expressed as below according to Derjaguin approximation.

$$F_{VW} = -\frac{1}{6} A r y^{-2} \qquad (5-1)$$

where A is the Hamaker coefficient, r is the radius of the analyte, y is the distance of the analyte from bottom wall.

The Hamaker coefficient A is approximately $1.68 \times 10^{-19}$ J for the PS particles in water [5-3]. The analyte is repulsed from wall by an electrostatic force $F_E$ and it is [5-4]

$$F_E = -16\kappa\varepsilon r \left(\frac{k_B T}{e}\right)^2 tanh\left(\frac{e\psi_w}{4k_B T}\right) tanh\left(\frac{e\psi_s}{4k_B T}\right) e^{-\kappa y} \qquad (5-2)$$

where $\kappa^{-1}$ is the Debye length, $\varepsilon$ is the dielectric permittivity of

water, $\psi_w$ and $\psi_s$ are the Stern potentials of wall and analyte, respectively.

The Debye length and the stern potential of the wall are assumed to be that $\kappa^{-1} \approx 150\ nm$ and $\psi_w \approx -50\ \mathrm{mV}$ according to the literature, respectively [5-5]. The stern potential of analytes is measured experimentally and its value is that $\psi_s \approx -67.3\ \mathrm{mV}$.

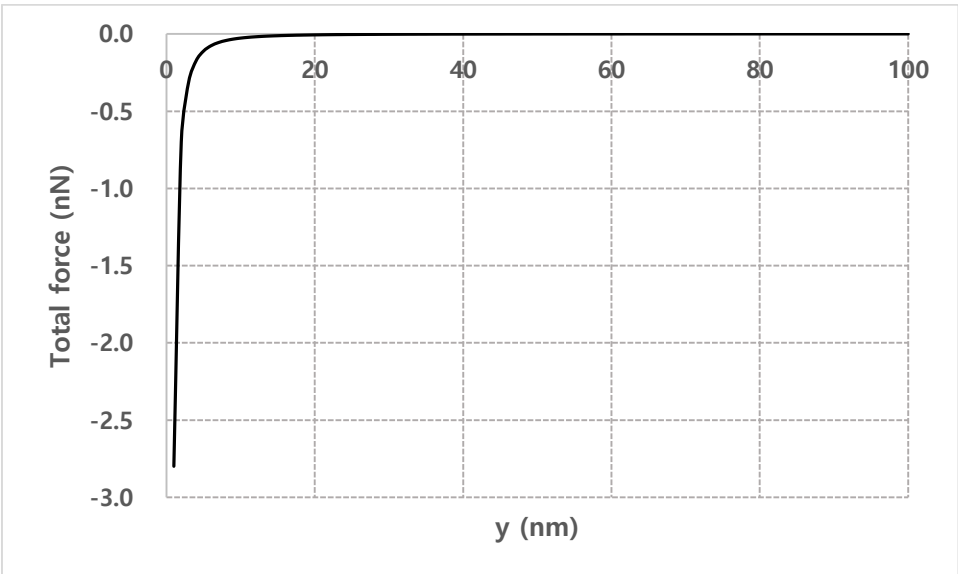


Figure 5-2. Total force exerted on analytes according to the distance from the bottom wall.

With Equation (5-1) and Equation (5-2), the total force exerted on analyte was calculated and is plotted in Figure 5-2. The total force is balanced at y=55.9 nm and the region for y<55.9 nm is assumed to be binding zone. For example, the analyte at y=55 nm is attracted to the wall with the value of $2.47 \times 10^{-14}$ nN and its terminal velocity in water is −13.1 μm/s, which was calculated using the Stokes' drag law. Time to reach terminal velocity is approximately 1 ps and time for the analyte to reach wall is 4.2 ms, thus, the particle at y<55.9 nm is bound to the wall in a few

milliseconds.

### 5.2.2. The number of analytes transported into the binding zone by dummy particles

Dummy particles induce lateral velocity not only towards the wall but also towards the channel center. Therefore, the particles outside the binding zone are not affected by dummy particles in terms of the binding phenomenon because the effect of dummy particles is canceled by its symmetry. But the particles within the binding zone cannot escape and moves towards the wall instantly, so the symmetry is broken inside the binding zone.

From the lateral velocity at the boundary for the binding zone (y=55.9 nm) induced by dummy particles, the total number of analyte transported in the binding zone can be calculated. Time for the dummy particle at y to pass through the microscopic area is $\Delta t(y) = W_1/u(y)$ (Figure 5−3a). Thus, the volume of fluid transported into the binding zone by a single dummy particle at y during $\Delta t$ is given as an integral form of $v_L$ as shown in Equation 5−3 (Figure 5−3b).

$$V_t = \Delta t \int \boldsymbol{v_L} \cdot \boldsymbol{dA} = \frac{W_1}{u} \int \boldsymbol{v_L} \cdot \boldsymbol{dA} \qquad (5-3)$$

where $\Delta t$ is the time for the dummy particle to pass through the microscopic area, $v_L$ is the lateral velocity at the boundary for binding zone induced by the dummy particle, $W_1$ is the length of the microscopic area, u is the x−directional speed of the dummy particle.

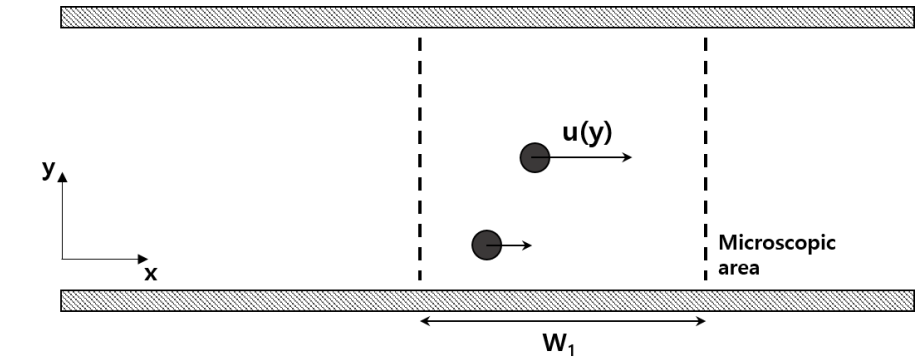


(a)

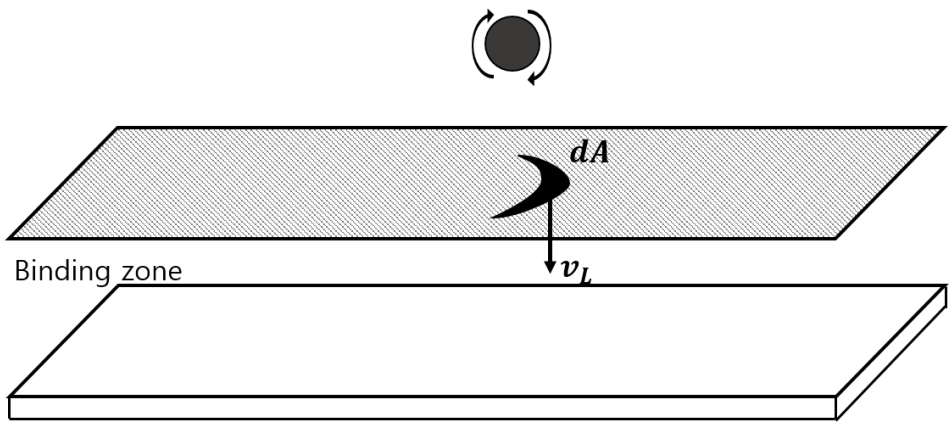


(b)

Figure 5−3. Schematic configuration for (a) time to pass through the microscopic area and (b) the lateral velocity at the boundary of the binding zone.

Assuming that analytes are dispersed uniformly, the number of analytes transported into the binding zone by the dummy particle at y is described using the number density of analytes as

$$N_{single}(\mathrm{y}) = \mathrm{n}V_t = \frac{nW_1}{u}\int \boldsymbol{v_L}\cdot\boldsymbol{dA} \qquad (5-4)$$

where n is the number density of analytes.

With the number density of dummy particles $n_d$, the total number of dummy particles passing through the microscopic area during the detection is

$$N_{dummy} = n_d W_2 \tau \int_0^H u(y) dy \quad (5-5)$$

where $n_d$ is the number density of dummy particles, $W_2$ is the width of the microscopic area, $\tau$ is the total detection time, H is the height of the channel.

Hence, the total number of analytes transported into the binding zone during detection is shown in Equation 5-6.

$$N = n_d W_2 \tau \int_0^H u(y) N_{single}(y) dy = n_d n W_1 W_2 \tau \int_0^H (\int \boldsymbol{v_L} \cdot \boldsymbol{dA})\, dy \quad (5-6)$$

## 5.3. Numerical simulation

### 5.3.1. Computational domain and boundary conditions for numerical simulation

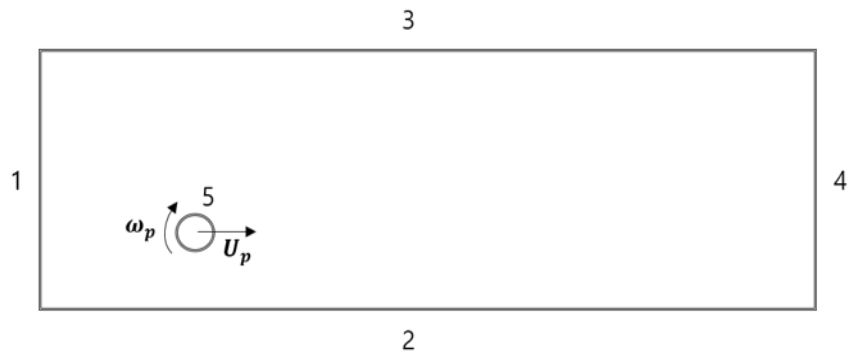


1 : Inlet
2 : No-slip wall, **u**=0
3 : No-slip wall, **u**=0
4 : Outlet
5 : Sliding wall (no-slip)

Figure 5-4. Computational domain and boundary conditions for numerical simulation.

Figure 5-4 shows a computational domain and boundary conditions for the numerical simulation. The flow is governed by the Navier-Stokes equations:

$$\rho\left(\frac{\partial \boldsymbol{u}}{\partial t}+\boldsymbol{u}\cdot\nabla\boldsymbol{u}\right)=-\nabla p+\mu\nabla^2\boldsymbol{u}+\frac{1}{3}\mu\nabla(\nabla\cdot\boldsymbol{u})+\rho\boldsymbol{g} \quad (5-7)$$

The left and right boundaries (1 and 4) of the simulation domain were set to be inlet and outlet, respectively with the fully developed flow condition in order that the entrance effect is not involved. No-slip condition was set on the top and bottom walls (2 and 3). Sliding wall with no-slip condition was applied on the particle surface (5), so the flow velocity at the particle surface is described as:

$$\mathbf{u}=\boldsymbol{U_p}+\boldsymbol{\omega_p}\times(\boldsymbol{r_s}-\boldsymbol{r_p}) \quad (5-8)$$

where $\boldsymbol{U_p}$ is the translational velocity of the particle, $\boldsymbol{\omega_p}$ is the rotational velocity of particle which is obtained by Equation 2, $\boldsymbol{r_s}$ and $\boldsymbol{r_p}$ are the position of particle surface and center, respectively.

$\boldsymbol{\omega_p}$ was calculated from the Jeffery model and $\boldsymbol{U_p}$ was set to an identical value with a flow velocity at the center of the particle. The numerical simulation was implemented in COMSOL Multiphysics 5.4 software with the above conditions.

### 5.3.2. Lateral velocity induced by dummy particles

In order to calculate the lateral velocity induced by dummy particles numerical simulation was performed under the method described in section 5.3.1 and the meshing for this model is shown in Figure 5-5. In order to examine the lateral velocity at the boundary for the binding zone, meshes at the wall were set to be 25 nm. At all

of the boundary layers, two layers of quad mesh were established. The number of elements was 60666, and the minimum element quality and average element quality were 0.3934 and 0.8539, respectively.

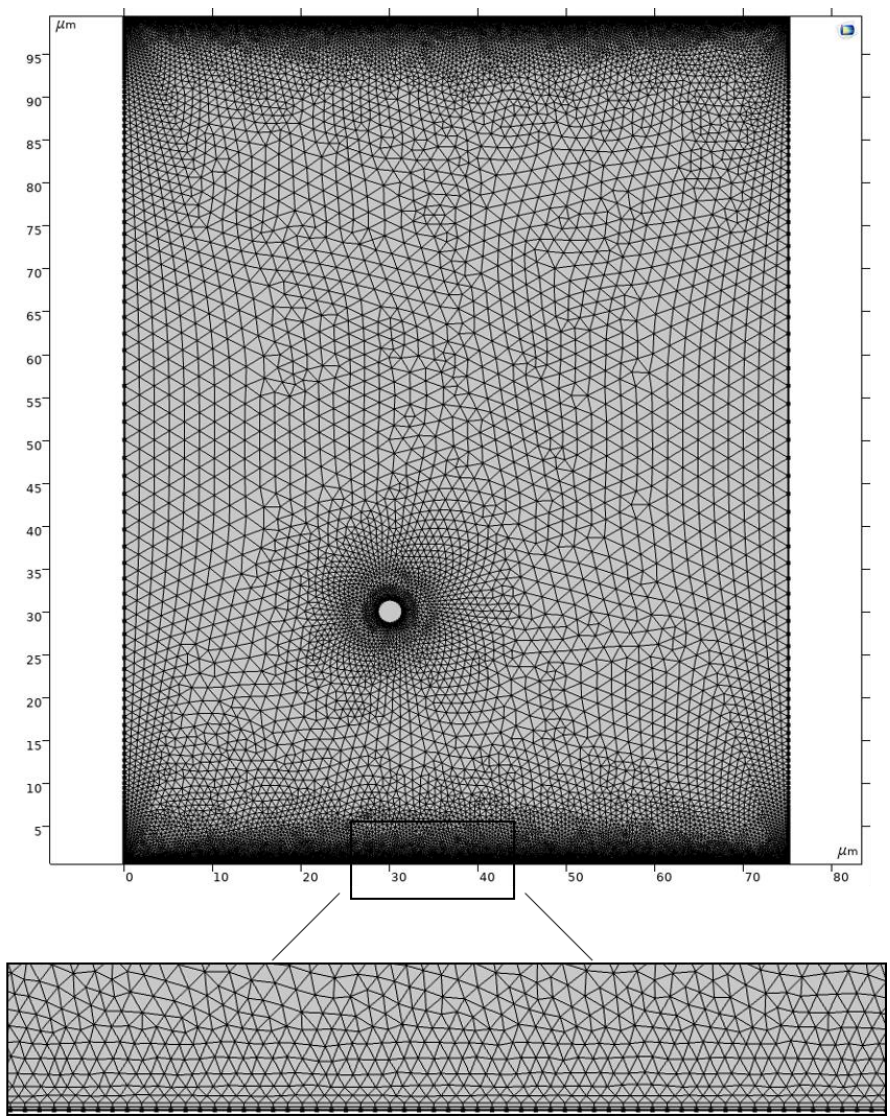


Figure 5-5. Meshing for the numerical simulation. Meshes at the wall were set to be 25 nm and two layers of quad mesh were established for boundary layer calculation.

Figure 5−6 is the simulation results for the velocity field of fluid with 3 μm dummy particle at y=20 μm. The velocity field is agitated around the dummy particle and lateral velocity is generated.

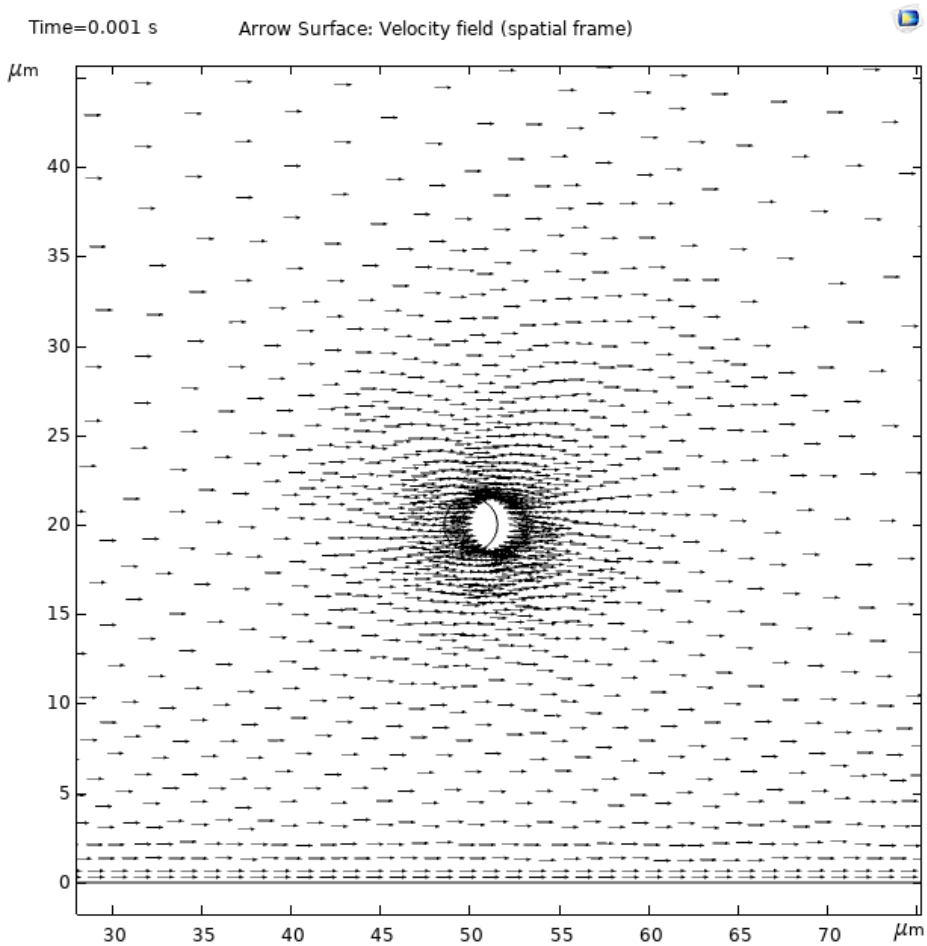


Figure 5−6. Simulation result for the velocity field with 3 μm dummy particle at y=20 μm (Flow rate=1.2 $mlh^{-1}$)

Figure 5−7 shows the simulation results for the lateral velocity at the boundary for the binding zone when the dummy particle is at y=2 μm. Substituting the values in Figure 5−7 to Equation (5−4) and assuming that the particle is cylindrical, the number of analytes transported into the binding zone by single dummy particle at y=2 μm is calculated : $N_{single}(y = 2\mu m) = 7.35 \times 10^4$

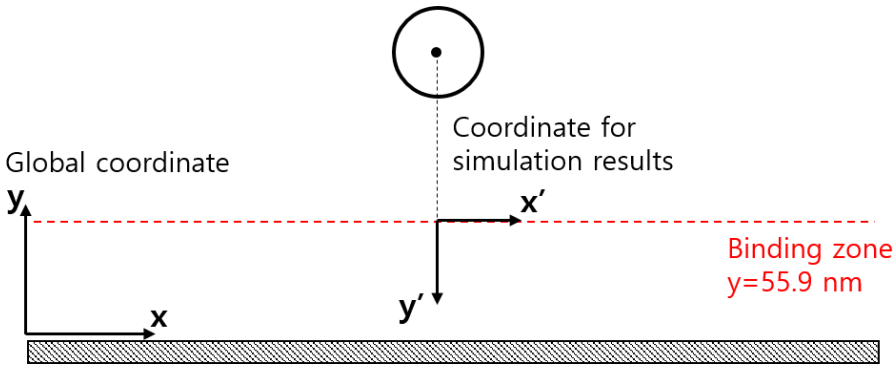


(a)

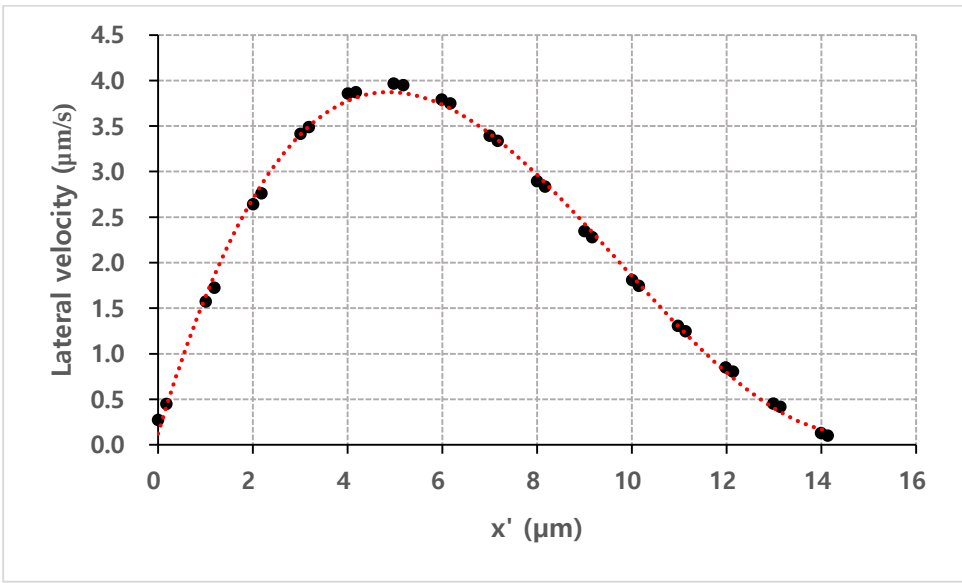


(b)

Figure 5−7. (a) The coordinate system for the results of numerical simulation, (b) Lateral velocity at the boundary for the binding zone for 3 μm dummy particle at y=2 μm. Circles indicate the simulation results and the dotted line is fitted graph for the simulation results.

Several calculations were repeated for different conditions and the results are shown in Figure 5−8. With this result and Equation 5−6, the total number of analytes enhanced by dummy particles can be calculated followed in the below section.

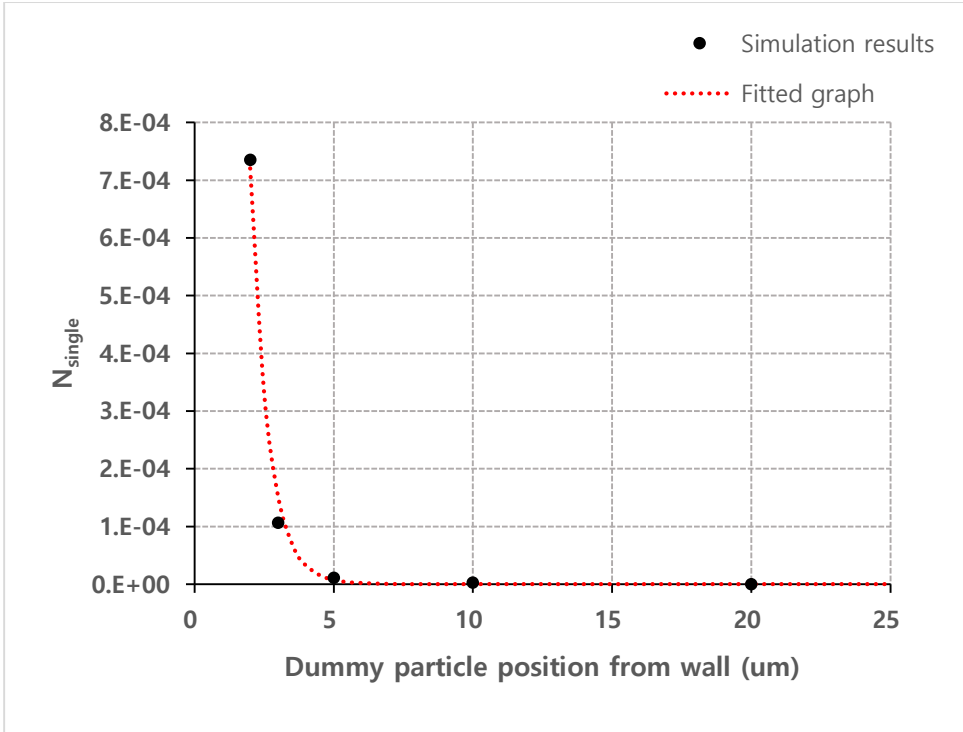


Figure 5-8. The number of analytes enhanced by a single dummy particle (Equation 5-4). Circles indicate the simulation results and the dotted line is fitted graph for the simulation results.

### 5.3.3. Numerical estimation for the number of bound particles

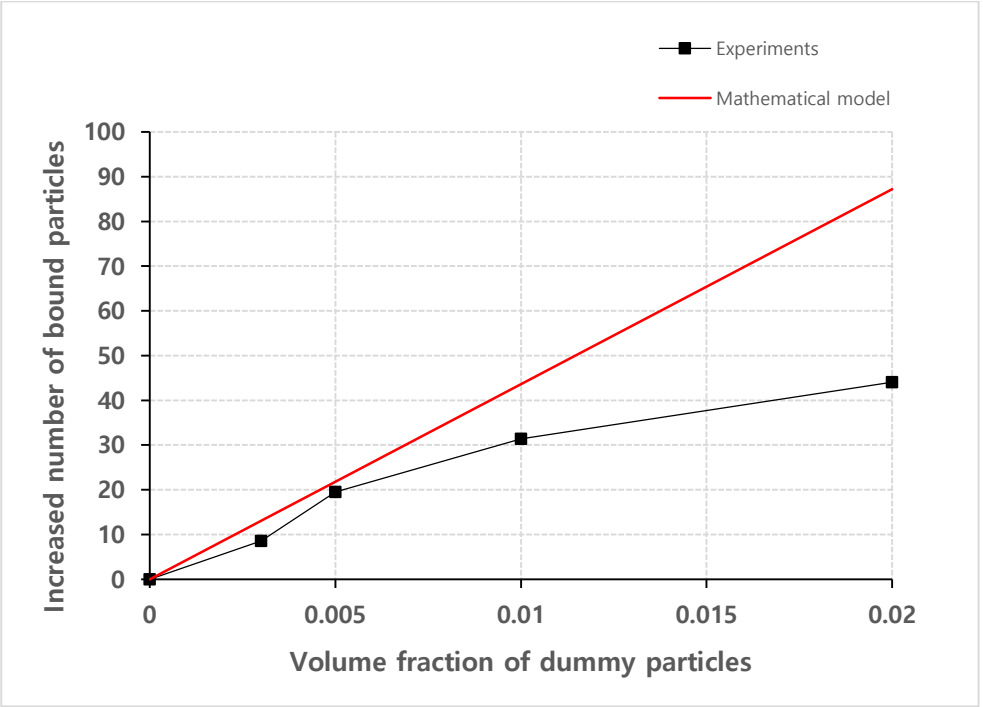


Figure 5−9. Increased number of bound particles according to 3 μm dummy particle volume fraction from experiments and mathematical model (number density of analytes n=$1.93 \times 10^{13}$ $m^{-3}$, Flow rate=1.2 $mlh^{-1}$, detection time $\tau$ =600 s).

Figure 5−9 shows the comparison for the increased number of bound particles from experiments and mathematical model in Equation (5−6). Considering that the dummy particle is assumed to be a cylinder in the mathematical model, the value from the mathematical model shows valid estimation until the volume fraction of dummy particles is 0.01. Because disturbance from adjacent particles is not reflected in the mathematical model, the values from the mathematical model show a linear trend. But the effect of dummy particles was saturated in experiments so the estimation deviates for the volume fraction of dummy particles over 0.01.

This phenomenon is shown in Figure 5-10, more clearly. As the interparticle distance between dummy particles decreases, the estimated value from the model starts to deviate.

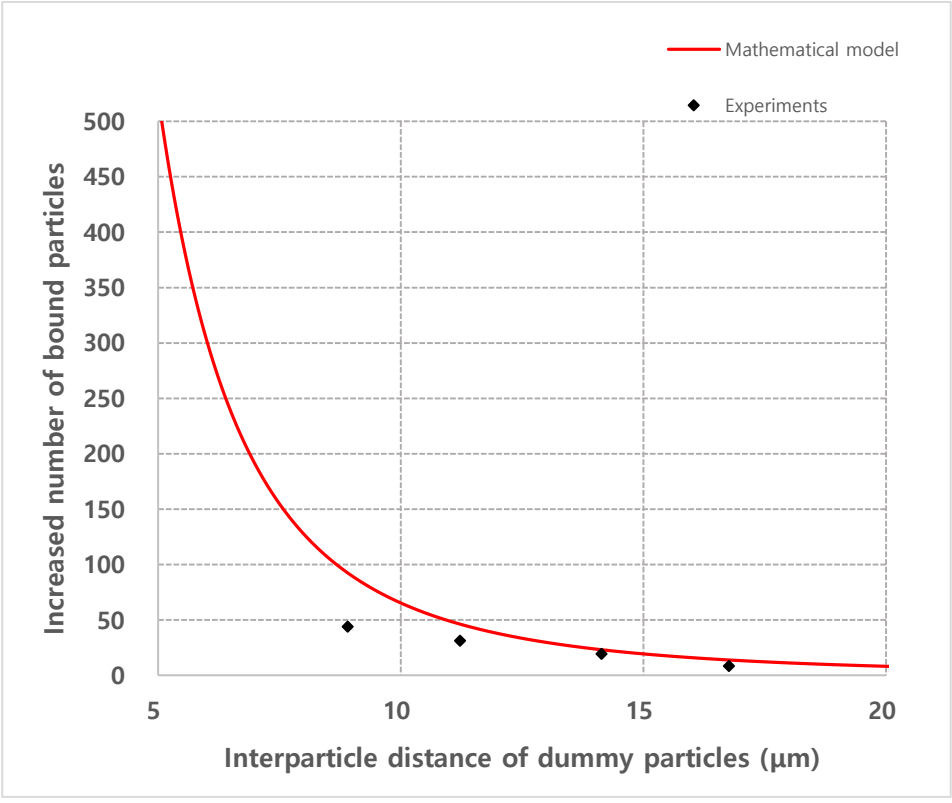


Figure 5-10. Increased number of bound particles according to the interparticle distance between 3 μm dummy particles from experiments and mathematical model (number density of analytes n=$1.93 \times 10^{13}$ $m^{-3}$, Flow rate=1.2 $mlh^{-1}$, detection time $\tau$ =600 s).

## Reference

[5-1] Poortinga, A. T.; Bos, R.; Norde, W.; Busscher, H. J., Electric double layer interactions in bacterial adhesion to surfaces. *Surface science reports* 2002, *47* (1), 1-32.

[5-2] Behrens, S. H.; Grier, D. G., Pair interaction of charged colloidal spheres near a charged wall. *Physical Review E* 2001, *64* (5), 050401.

[5-3] Ottewill, R.; Shaw, J., Stability of monodisperse polystyrene latex dispersions of various sizes. *Discussions of the Faraday Society* 1966, *42*, 154-163.

[5-4] Zheng, X.; Silber-Li, Z., The influence of Saffman lift force on nanoparticle concentration distribution near a wall. *Applied physics letters* 2009, *95* (12), 124105.

[5-5] Bouzigues, C.; Tabeling, P.; Bocquet, L., Nanofluidics in the debye layer at hydrophilic and hydrophobic surfaces. *Physical Review Letters* 2008, *101* (11), 114503.